HHS Public Access

Author manuscript

Cell Rep. Author manuscript; available in PMC 2021 June 07.

Published in final edited form as:

Cell Rep. 2021 May 11; 35(6): 109098. doi:10.1016/j.celrep.2021.109098.

Persistent NF-κB activation in muscle stem cells induces proliferation-independent telomere shortening

Elisia D. Tichy[1], **Nuoying Ma**[1], **David Sidibe**[1], **Emanuele Loro**[2], **Jacob Kocan**[1], **Delia Z. Chen**[1], **Tejvir S. Khurana**[2], **Paul Hasty**[3], **Foteini Mourkioti**[1,4,5,6,*]

[1]Department of Orthopaedic Surgery, Perelman School of Medicine, The University of Pennsylvania, Philadelphia, PA 19104, USA

[2]Department of Physiology and Pennsylvania Muscle Institute, Perelman School of Medicine, The University of Pennsylvania, Philadelphia, PA 19104, USA

[3]The Sam and Ann Barshop Institute for Longevity and Aging Studies, UT Health Science Center at San Antonio, San Antonio, TX 78229, USA

[4]Department of Cell and Developmental Biology, Perelman School of Medicine, The University of Pennsylvania, Philadelphia, PA 19104, USA

[5]Institute of Regenerative Medicine, Musculoskeletal Regeneration Program, Perelman School of Medicine, The University of Pennsylvania, Philadelphia, PA 19104, USA

[6]Lead contact

SUMMARY

During the repeated cycles of damage and repair in many muscle disorders, including Duchenne muscular dystrophy (DMD), the muscle stem cell (MuSC) pool becomes less efficient at responding to and repairing damage. The underlying mechanism of such stem cell dysfunction is not fully known. Here, we demonstrate that the distinct early telomere shortening of diseased MuSCs in both mice and young DMD patients is associated with aberrant NF-κB activation. We find that prolonged NF-κB activation in MuSCs in chronic injuries leads to shortened telomeres and Ku80 dysregulation and results in severe skeletal muscle defects. Our studies provide evidence of a role for NF-κB in regulating stem-cell-specific telomere length, independently of cell replication, and could be a congruent mechanism that is applicable to additional tissues and/or diseases characterized by systemic chronic inflammation.

In brief

*Correspondence: fmour@pennmedicine.upenn.edu.

AUTHOR CONTRIBUTIONS

E.D.T., N.M., D.S., J.K., and D.Z.C. performed experiments and analyzed data. E.L. and T.S.K. performed and analyzed force measurements. P.H. provided the $Ku80^{+/-}$ mice. E.D.T. and F.M. designed experiments, interpreted data, and wrote the manuscript.

DECLARATION OF INTERESTS

The authors declare no competing interests.

SUPPLEMENTAL INFORMATION

Supplemental information can be found online at https://doi.org/10.1016/j.celrep.2021.109098.

Tichy et al. reveal a role for NF-κB signaling in regulating telomere length in muscle stem cells (MuSCs) after chronic injuries. Persistent activation of NF-κB leads to shortened telomeres, Ku80 dysregulation, and muscle defects. The findings link stem cell dysfunction and NF-κB-dependent telomere shortening in Duchenne muscular dystrophy.

Graphical Abstract

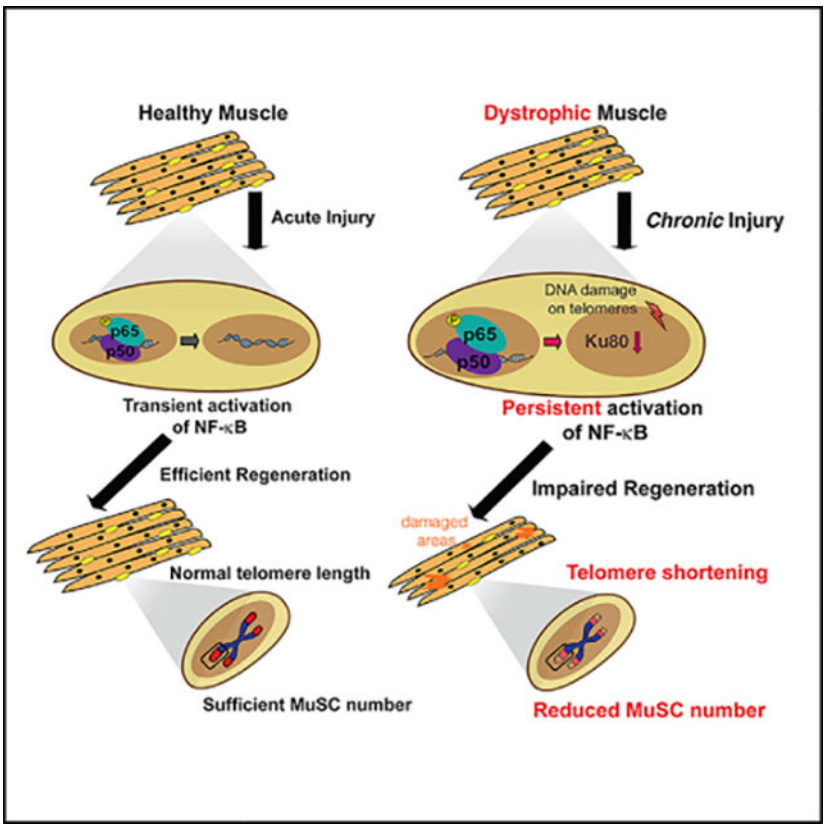

INTRODUCTION

The stages of skeletal muscle regeneration are well characterized following injury, starting with necrosis of damaged muscle tissue and the infiltration of immune cells (Frenette et al., 2000; Tidball, 2005). Inflammatory signals both directly and indirectly lead to activation of resident muscle stem cells (MuSCs; also called satellite cells), which respond to muscle damage by population expansion, followed by selective differentiation into myogenic progeny (Chazaud et al., 2003; Tidball and Wehling-Henricks, 2015).

Duchenne muscular dystrophy (DMD) is a fatal X-linked degenerative muscle disease, and it is among the most common lethally inherited disorders in children (Emery, 2002). DMD is caused by mutations in the *dystrophin* gene, which codes for a cytoskeletal protein that acts as a crucial bridging protein between the sarcomere and extracellular matrix (Hoffman et al., 1987). The complete or partial loss of dystrophin in muscular dystrophies impairs the ability of the muscle to contract and causes the muscle to break down. This acts as constant injury

to the muscle that progressively affects the MuSC pool (Morgan and Zammit, 2010; Sacco et al., 2010), presumably due to an autonomous dysfunction (Dumont et al., 2015). Thus, MuSC function is severely affected in DMD, and although the disease is initiated by dystrophin deficiency, it is ultimately a stem cell disease (Dumont et al., 2015; Sacco et al., 2010). Previous work showed that accelerated telomere shortening occurs in muscular dystrophy in both skeletal muscle and cardiomyopathy (Mourkioti et al., 2013; Sacco et al., 2010). Recent studies have also revealed that MuSCs derived either from dystrophic mice or young DMD patients exhibit critically shortened telomeres early on during disease progression (Tichy et al., 2017). These observations suggest that modulation or maintenance of MuSC function can prevent or diminish destructive muscle processes in chronic injury conditions. However, the molecular mechanisms contributing to MuSC-specific telomere shortening are currently unknown.

Here, we show that persistent activation of nuclear factor kb (NF-κB) leads to telomere shortening in MuSCs under chronic injury conditions, and it is independent of proliferation. Instead, this mechanism involves Ku80 dysregulation and increased DNA damage, specifically on telomeres, that results in MuSC loss and, subsequently, skeletal muscle regenerative failure. Overall, our findings propose a previously unrecognized role of NF-κB in regulating MuSC dysfunction by affecting telomeres, a key event during the progression of DMD.

RESULTS

NF-κB is dysregulated in dystrophic MuSCs

To understand the mechanisms that affect telomere length and function in diseased MuSCs, we assayed their internal signaling pathways by flow cytometry (Table S1). We found that a higher proportion of the MuSCs from dystrophic mice exhibited higher NF-κB activation (Figure 1A) and accumulation of p-p65 (Figures 1B and 1C). We expanded upon these observations by assessing the timing of NF-κB activation following a single intramuscular injury. Muscle injury rapidly increases NF-κB activation in MuSCs (Figure 1D). But in dystrophic mice, p-p65+ MuSCs are more numerous at all time points, including baseline conditions (Figure 1D). Hence, the inherent endogenous injuries observed in dystrophic mice induce a constant elevated NF-κB signaling response in MuSCs.

MuSC-specific NF-κB activation does not alter muscles in non-injured conditions

To examine the *in vivo* impact of persistent NF-κB activation in regulating telomere length in MuSCs during chronic injury, we generated a mouse that allows expression of a constitutively active (CA) form of the *IKK2* gene (Calado et al., 2010) specifically in MuSCs (Pax7^{ERT2Cre}/IKK2CA or IKK2CA^{MuSC}) (Figure S1A). To generate mice in which NF-κB signaling is abrogated in MuSCs, we crossed mice carrying a floxed allele of the NF-κB regulator *NEMO* (Schmidt-Supprian et al., 2000) with the same Pax7^{ERT2Cre} mice (Murphy et al., 2011) to generate NEMO knockout (NEMOKO^{MuSC}) mice. Characterization of these mice demonstrates that we obtained >90% Cre recombination efficiency after seven daily intraperitoneal tamoxifen injections, which resulted in significant upregulation of the IKK2 gene in IKK2CA^{MuSC} mice and downregulation in NEMOKO^{MuSC} mice (Figure

S1B). The above genetic approaches allow for CA or inactivation of p65 in MuSCs, as shown by flow cytometry analysis (Figure 2A). Enforced expression of activated IKK2 alone or ablation of NEMO in MuSCs had no effect on muscle morphology (Figure S1C), muscle size (Figure S1D), function (Figure S1E), and/or telomere length (Figure S1F) under steady-state conditions. These data suggest that in the absence of injury, persistent activation of MuSC-specific NF-κB has minimal effects in skeletal muscles.

Rapid telomere shortening in injured MuSCs with persistent NF-κB

To investigate the importance of injury in NF-κB-dependent telomere length regulation and to mimic the rounds of degeneration/regeneration occurring in the dystrophic condition (Morgan and Zammit, 2010), we implemented a multiple injury model in control, IKK2CA^{MuSC}, and NEMOKO^{MuSC} mice (Figure 2B). Assessment of telomere lengths of MuSCs isolated from these mice by MuQ-FISH (fluorescence *in situ* hybridization) (Tichy et al., 2017) uncovered a propensity of telomere shortening in IKK2CA^{MuSC}-derived MuSCs (Figure 2C). However, NEMOKO^{MuSC} MuSCs have unaltered telomere lengths even after many injuries (Figure 2C), demonstrating that NF-kB inhibition maintains telomere length. These findings further suggest that NF-κB activation is required for telomere shortening in injured muscles, providing strong support that prolonged NF-κB activation drives telomere shortening under chronic injuries. Interestingly, telomeres start to shorten after three injuries in IKK2CA^{MuSC} cells, but this reduction becomes more severe with an increasing number of injuries (Figures 2D–2F and S2A). Moreover, the progressive telomere shortening observed after an increased number of injuries correlates well with the worsening histology (Figures 2G–2I) and fibrosis (Figures S2B and S2C) in IKK2CA^{MuSC} muscles with an increased number of injuries. These studies support the notion that NF-κB-dependent telomere shortening contributes to the histopathology in skeletal muscles under repetitive injuries. Altogether, these data demonstrate an unconventional role for unrestrained NF-κB signaling in MuSCs to promote telomere attrition and impairment of regeneration under chronic injury conditions.

Telomere shortening in MuSCs is not caused by enhanced proliferation

In proliferative cells, DNA polymerases fail to completely replicate telomeres following each cell division, which eventually leads to critical telomere shortening (Lee et al., 1998). To address whether the rapid MuSC-specific telomere shortening observed in injured IKK2CA^{MuSC} mice was caused by MuSC proliferative changes, we injured control or IKK2CA^{MuSC} mice repeatedly. At 3 days after the last injury, a timepoint considered the peak of MuSC proliferation (Morgan and Zammit, 2010), mice were pulsed *in vivo* with the nucleotide analog 5-ethynyl-2′-deoxyuridine (EdU) to label cells undergoing DNA replication (Figure 3A). In uninjured muscles, only a small portion of MuSCs was EdU^{+} (Figures 3B and 3C), consistent with the notion that adult MuSCs with higher NF-kB activation are largely quiescent under steady-state conditions. Interestingly, upon injury, both control and IKK2CA^{MuSC} MuSCs were proliferating at comparable rates (Figures 3B and 3C). Similarly, an equivalent level of the proliferation marker Ki67, in combination with the stem cell marker Pax7 was found in injured control and IKK2CA^{MuSC} muscles (Figures 3D and 3E). To ensure that the window of optimal *in vivo* proliferation was not missed by our previous assessments, as well as to confirm a large enough window of EdU incorporation

was included, EdU was administered daily, for a total of three times, and MuSCs were harvested 3 or 5 days after the last injury (Figure 3F). Similar to the previous data, no significant increases in proliferation were evident in IKK2CA^{MuSC} MuSCs (Figure 3G). We conclude that in contrast to other cell types (Sasaki et al., 2006), the constant activation of NF-κB in MuSCs does not result in higher rates of proliferation even under injury conditions. Altogether, these data unequivocally demonstrate a proliferation-independent mechanism of NF-κB to drive MuSC-specific telomere shortening.

NF-κB regulates Ku80 expression in MuSCs in chronic muscle injuries

Telomeres are not naked DNA but are instead associated with six proteins, called shelterins (TIN2, TPP1, POT1, RAP1, TRF1, and TRF2) (de Lange, 2005; Hsu et al., 1999), together with the DNA-binding proteins Kus (de Lange, 2005; Hsu et al., 1999) (Figure S4A). To delineate alternative mechanisms to rationalize the observed telomere shortening in IKK2CA^{MuSC} MuSCs experiencing chronic injuries, we carried out *in-silico* analysis on promoters of genes, whose proteins are known to reside at telomeres. Given that Kus bind to telomeres, aid the localization of other shelterins, and regulate telomere length, we included them in our *in-silico* analysis (de Lange, 2005; Hsu et al., 1999). NF-κB functions by binding to promoter and enhancer regions containing kB sites to regulate gene expression (Dong et al., 2008; Hayden and Ghosh, 2004). We found that proteins bound to telomeric DNA contain kB sites in their promoters (Table S2), raising the intriguing possibility that NF-κB-dependent regulation of telomere binding proteins may have a significant impact on telomere length in MuSCs. We then performed qRT-PCR to validate the *in-silico* analysis and detected downregulation of telomeric XRCC5/Ku80 gene expression in MuSCs from injured muscles (Figure 4A), while all other telomeric genes had no significant differences (Figure 4A). Similarly, we found downregulation of Ku80 protein in MuSCs from IKK2CA^{MuSC} muscles after 3× injury (Figures 4B and 4C), further demonstrating the NF-κB-dependent regulation of Ku80. In addition, we found undetectable *tert* levels in wild-type (WT) or IKK2CA^{MuSC} MuSCs either in steady-state or upon injury conditions (Figure S3B). Since tert transcripts are detectable in embryonic stem cells (ESCs) within the same reaction (technical control), our data suggest that *tert* is either present at very low (undetectable) levels or expressed transiently in freshly isolated MuSCs, in contrast to what is known for cancer cell lines (Yin et al., 2000; Zuo et al., 2011). Importantly, Ku80 levels are unchanged in both IKK2CA uninjured MuSCs (Figure S3C; NF-κB activation alone without injury) and MuSCs from NEMOKO^{MuSC} injured mice (Figure S3D; injury combined with NF-κB inactivation in MuSCs), demonstrating that NF-κB is required during injury to alter Ku80 levels (Figures 4B and 4C) and induce telomere shortening (Figures 2C–2F). Overall, these data indicate a previously unrecognized requirement of NF-κB in regulating Ku80 expression associated with telomere length in freshly isolated MuSCs from injured muscles.

MuSC telomere shortening leads to increased DNA damage in telomeres and stem cell exhaustion over time

In mammalian cells, DNA damage, in the form of double-stranded DNA breaks, is typically repaired by non-homologous end-joining (NHEJ) (Mao et al., 2008) and depends on the activity of Ku80 to recognize damaged DNA ends (Koike and Koike, 2008). Indeed, we

observed a higher number of centralized nuclei in regenerating IKK2CA^{MuSC} fibers that positively stained for the DNA damage marker 53BP1 (Figures S3E and S3F). Extensive telomere shortening can be recognized by DNA damage sensors as free DNA ends (Hsu et al., 2000). In fact, we did observe increased numbers of telomere-induced foci (TIFs) in chronically injured IKK2CA^{MuSC} MuSCs (Figures 4D and 4E), as identified by the stem cell marker, vascular cell adhesion molecule (VCAM) (Figure S3G). These data are in agreement with the notion that telomere dysfunction is governed by proteins that also control DNA damage response (Takai et al., 2003).

To further investigate the *in vivo* consequence of the early telomere shortening in MuSCs in chronic injury, we crossed the MuSC-specific IKK2CA^{MuSC} mice with Pax7EGFP reporter mice, which express EGFP under the control of the Pax7 promoter (Tichy et al., 2018). The Pax7EGFP/IKK2CA^{MuSC} mouse allows for direct visualization and evaluation of MuSCs in their native environment on all fibers within the same animal in a spatiotemporal manner. Utilizing this method, we assessed the number of MuSCs by two-photon microscopy following chronic injury and recovery. We found that the number of MuSCs decreases over time in Pax7EGFP/IKK2CA^{MuSC} skeletal muscles (Figure 4F), indicative of an exhaustion of the stem cell pool under chronic injury.

MuSC-specific NF-κB activation exacerbates the dystrophic muscle defects

To explore whether MuSC-specific activation of NF-κB could exacerbate the progression of dystrophy, we crossed IKK 2CA^{MuSC} mice with a dystrophin mutant mouse (Im et al., 1996). The resulting double mutants are designated herein as mdx/IKK2CA^{MuSC}. These mice have higher muscle damage, shown by the levels of creatine kinase (Figure 5A), an established damage diagnostic indicator in DMD (Zatz et al., 1991). The severity of muscle defects in mdx/IKK2CA^{MuSC} mice is consistent with reduced muscle weight (Figures S4A and S4B), worse muscle morphology (Figure S4C), and reduced area of fibers with centralized nuclei (Figure S4D). Interestingly, we observed substantial kyphosis (Figure 5B), a classical clinical manifestation of DMD due to weakness of trunk muscles (Oda et al., 1993; Wilkins and Gibson, 1976) and impaired muscle performance in mdx/IKK2CA^{MuSC} mice compared to mdx controls (Figures 5C and 5D). Importantly, MuSCs isolated from mdx/IKK2CA^{MuSC} mice exhibited higher levels of p65 (Figure 5E), demonstrated shortened telomeres (Figures 5F and S4E), exhibited increased numbers of TIFs (Figure 5G), and had a reduced number of MuSCs (Figure S4F). We conclude that the persistent activation of NF-κB in MuSCs in the context of repetitive injuries as caused by the lack of dystrophin leads to the aggravation of the mdx phenotype, imitating the human disease.

Downregulation of Ku80 alone or in the context of chronic injuries reduces telomere length in MuSCs

To gain more insight into the involvement of Ku80 in telomere shortening in myogenic cells, we first investigated telomere length in the C2C12 mouse myoblast cell line (Figure S5A). Using short hairpin RNA (shRNA) vectors targeting *XRCC5*, which encodes the Ku80 protein, we observed significant knockdown at the protein level when compared to cells transfected with empty vector (Figure S5B). Upon performing MuQ-FISH, we uncovered that Ku80 downregulation is sufficient to induce telomere shortening in myogenic cells with

two different shRNAs (Figures S5C and S5D). These data demonstrate that downregulation of Ku80 alone is sufficient to reduce telomere length in myogenic cells. Next, we extended our findings by investigating the effect of Ku80 manipulation on telomere length *in vivo*, utilizing a Ku80 heterozygous mouse line (Zhu et al., 1996). We found that MuSCs derived from this mouse exhibited only ~20% reduction of Ku80 protein expression compared to Ku80 WT littermates (Figure S5E). Nevertheless, we still observed a reduction in telomere lengths of these Ku80 heterozygous mice after 3× injury (Figure S5F), suggesting that even a mild reduction of Ku80 protein is sufficient to shorten telomeres in MuSCs. To further demonstrate the involvement of Ku80 in telomere length modulation *in vivo* in more severe chronic injuries, we bred mdx mice with $Ku80^{+/-}$ mice. Interestingly, MuSCs in the mdx/$Ku80^{+/-}$ muscles have a pronounced shift toward shorter telomeres (Figure S5G), increased muscle damage (Figure S5H), and impaired muscle performance (Figure S5I). These data suggest that the mdx/$Ku80^{+/-}$ mice exhibit similar muscle defects as the ones seen in mdx/$IKK2CA^{MuSC}$ mice (Figure 5). Altogether, these results demonstrate that Ku80 is a major regulator of telomere length in myogenic cells, both *in vitro* and *in vivo*, either alone or in the context of dystrophy.

Ku80 dysregulation and telomere damage in human dystrophic MuSCs

We next investigated whether our mouse findings recapitulate what happens in the human dystrophic condition. We found that human DMD MuSCs express significantly higher levels of p-p65 (Figures 6A and 6B), and a larger portion is localized in the nucleus (Figure 6C), further supporting the notion of persistent elevated NF-κB signaling in dystrophic human MuSCs. Interestingly, human DMD MuSCs have significantly decreased Ku80 levels (Figures 6D and 6E), as shown by immunohistochemistry analysis on human muscles from DMD patients. Furthermore, in corroboration with the mouse data, we found shortened telomeres (Figure 6F), higher levels of DNA damage (Figures S6A and S6B), and increased numbers of TIFs (Figures 6G and 6H) in human diseased MuSCs compared to aged-matched healthy controls. Altogether, these striking human findings, which are consistent with the mouse results, provide further evidence that persistent NF-κB activation specifically in MuSCs leads to Ku80 dysregulation and predisposes these cells to premature telomere shortening and an increased number of TIFs that ultimately contribute to the severe dystrophic skeletal muscle phenotype.

DISCUSSION

Previous work had revealed that MuSCs progressively become dysfunctional in dystrophy, and telomere shortening is a major hallmark of the disease (Dumont et al., 2015; Sacco et al., 2010; Tichy et al., 2017). Here, we provide evidence of the *in vivo* molecular basis for telomere shortening of stem cells under chronic injury conditions. These findings provide insights into the fundamental regulatory mechanisms of MuSC-specific telomere shortening under chronic injuries.

Indications of perturbation of NF-κB signaling exist in various muscle diseases, such as muscle atrophy conditions (Cai et al., 2004; Mourkioti et al., 2006; Mourkioti and Rosenthal, 2008), cancer cachexia (He et al., 2013), dystrophinopathies such as Limb-girdle

muscular dystrophy type 2A (LGMD2A) (Baghdiguian et al., 1999), and DMD (Acharyya et al., 2007; Hammers et al., 2016; Messina et al., 2011). In addition to its role in regulating myogenesis (Mourkioti and Rosenthal, 2008), NF-κB is likely to modulate immune responses, muscle damage, and repair in DMD as well as in other muscle disorders. However, the survival effect of NF-κB in LGMD2A muscles, compared with its rather negative contribution in DMD, reflects the complexity of this pathway in chronic muscle diseases. Previous genetically modified animal models generated to interfere with NF-κB signaling only assessed NF-κB function regarding cancer cachexia (He et al., 2013) and aging (Oh et al., 2016; Proto et al., 2017).

By targeting the MuSC compartment in adult mice, we demonstrate that the inherent endogenous injuries observed in dystrophic mice induce a constant elevated NF-κB signaling response in MuSCs in both mdx and, most importantly, in human DMD MuSCs. Furthermore, we showed that persistent MuSC-specific NF-κB activation in injured muscles leads to telomere shortening and impairment of regeneration, as shown by the worsened histopathology of skeletal muscles during the progression of the chronic injury.

Additionally, we demonstrate that persistent MuSC-specific NF-κB activation in injured muscles drives telomere shortening via a mechanism that does not raise proliferation levels. Instead, we describe an NF-κB-dependent Ku80 dysregulation and increased DNA damage on telomeres in MuSCs from both dystrophic mice and human patients. While the effects of Ku80 in NHEJ are well documented (Fell and Schild-Poulter, 2015), its potential mechanistic involvement in telomere length alteration is less clear. Indeed, the absence of Ku80 has been associated with both telomere lengthening and shortening, depending on the cell line used; the organism (i.e., yeast, *Drosophila*, mouse, plant); or the context (embryonic development, cancer, or aging) (Boulton and Jackson, 1998; Chai et al., 2002; d'Adda di Fagagna et al., 2001; Didier et al., 2012; Espejel et al., 2004; Gallego et al., 2003; Indiviglio and Bertuch, 2009; Li et al., 2007; Melnikova et al., 2005). Furthermore, it is still unclear when Ku80 could function alone or as a heterodimer of both Ku80 and Ku70 subunits (Fell and Schild-Poulter, 2015). It was previously shown that loss of a single allele of Ku80 leads to dysfunction of muscle-derived cells and accelerated aging (Didier et al., 2012). In this study, we demonstrate that NF-κB regulates Ku80 expression in MuSCs in chronic muscle injuries and dystrophic muscles in both mouse and human. This NF-kB-dependent *in vivo* telomere regulatory mechanism is different from the modulation of telomeric proteins Tert or Rap1 that have been shown in cancer cells (Teo et al., 2010; Yin et al., 2000; Zuo et al., 2011). Additional work, to generate more targeted molecular tools for Kus and to investigate the exact role of Ku80 in the regulation of telomere integrity (Indiviglio and Bertuch, 2009), will be instrumental in order to identify other contributing molecular mechanisms and to develop concepts that could maintain MuSC telomere length under injured conditions.

It has been suggested that MuSCs could not keep up with the high regeneration demand under chronic injury conditions (Sacco et al., 2010). However, other studies have shown that MuSC numbers are elevated in mdx muscles in mice or DMD patients (Boldrin et al., 2015; Dumont et al., 2015; Kottlors and Kirschner, 2010). All these studies were dependent on prospective cell isolation methods, which rely on enzymatic digestion efficiency, using fluorescence-activated cell sorting (FACS) based on cell-surface markers (Tichy et al., 2017)

or *ex vivo* methods to isolate single muscle fibers, in combination with Pax7 antibody staining (Sacco et al., 2010). Both methods result in cell loss due to either incomplete tissue digestion and/or cell death during these long procedures, and the cell loss is likely exacerbated in diseased muscles that are inherently more fibrotic and fragile. Additionally, only the intact/non-broken fibers are used for quantification and, therefore, single-fiber isolation selects for MuSC measurements in somewhat "healthier" fibers. To overcome these limitations and to evaluate the consequences of telomere shortening in MuSCs, we used the Pax7EGFP reporter mouse (Tichy et al., 2018) to study changes in the number of MuSCs during disease conditions. Our analysis revealed that there is a loss of MuSC over time in both the IKK2CA^{MuSC} after repetitive injuries and the mdx/IKK2CA^{MuSC} mice, which contributes to the muscle regeneration impairment seen in the context of chronic injuries as caused by the lack of dystrophin.

In summary, this study establishes a link between stem cell functional exhaustion and NF-κB-dependent telomere shortening. Our data suggest that maintaining telomere length of MuSCs could boost the regenerative ability of MuSCs in disease-related chronic injuries such as DMD. It was recently proposed that chronic inflammation can accelerate aging via exacerbation of telomere dysfunction in multiple tissues (Jurk et al., 2014). Therefore, the molecular mechanism presented here for DMD could also be a more generalized mechanism that lowers regenerative potential in other tissues with systemic chronic inflammation and/or accelerates normal and pathological aging.

STAR★METHODS

RESOURCE AVAILABILITY

Lead contact—Further information and requests for resources and reagents should be directed to and will be fulfilled by the Lead Contact, Dr. Foteini Mourkioti (fmour@pennmedicine.upenn.edu)

Materials availability—All unique/stable reagents generated in this study are available from the Lead Contact with a completed Materials Transfer Agreement.

Data and code availability statement—This study did not generate any unique datasets or code.

EXPERIMENTAL MODELS AND SUBJECT DETAILS

Animals—All animals were housed and bred in accordance with the University of Pennsylvania IACUC guidelines. Mice used in this study include C57BL/6 (Jackson Labs-JAX Stock #000664), IKK2 constitutively active mice (IKK2CA); breeding of JAX stock 008242 for Lox-stop-Lox IKK2CA and Pax^{ERT2CRE} (JAX Stock #017763) (Murphy et al., 2011), mdx4^{cv} mice (JAX stock #002378), or mdx^{4cv} bred to IKK2CA. NEMO floxed mice and genotyping protocols were a gift from Dr. Pasparakis. Ku80+/− mice were a gift from Dr. Hasty. For several experiments, Pax7EGFP mice were bred to the aforementioned mouse lines. Mice were genotyped according to established protocols using ear punches as starting material. To induce Cre expression, mice were injected with 250uL tamoxifen (Sigma;

20mg/mL in ethanol/corn oil in a 1/10 ratio) IP twice weekly for a total of 7 injections, starting at 6 to 8 weeks of age. For all experiments, mice of the same sex and similar age were compared. The age of mice for each experiment is reported in Figure Legends.

Chronic induced injury—Muscles were injured with 10 μg/mL notexin (Latoxan) weekly. The tibialis anterior (TA), gastrocnemius, and quadriceps muscles of one hind limb were injured with 10 μL (TA) or 20 μL (gastrocnemius and quadriceps) notexin. Muscles were collected post-injury at three days (for MuSC isolation) or at seven days (for staining with Hematoxylin and Eosin).

Human samples—Human samples were a gift from Dr. Sacco (Tichy et al., 2017). Human muscle biopsies from healthy and DMD patients were obtained from the lower extremity muscles during surgical procedures as part of the patient's clinical care plan at Rady's Children's Hospital, San Diego. Written informed consent from patients, parent or guardian was obtained for all subjects. The protocol was approved by the University of California, San Diego Human Research Protectants Program and Institutional Review Board in accordance with the requirements of the Code of Federal Regulations on the Protection of Human Subjects. All materials were collected from de-identified males.

METHOD DETAILS

Muscle stem cell isolation—MuSCs were FACS-isolated as previously described (Tichy et al., 2017). Briefly mice were sacrificed, and the tibialis anterior, quadriceps and gastrocnemius muscles were dissected from both hind limbs. Muscle was finely minced and placed in a C tube (Miltenyi) containing 0.15% collagenase in 10 mL DMEM. Tubes were loaded into a MACS Dissociator (Miltenyi) and the manufacturer's muscle-01 program was run. Tubes were incubated in at 37°C for 30 min, subjected to the muscle-01 program again, and incubated at 37°C for an additional 30min. Seventy-five microliters of 2% collagenase (Sigma-Aldrich) and 75 μL of 4.8 U/mL dispase (Roche) was added, and tubes were vortexed at maximum speed prior to a 30min incubation at 37°C. Cells were passed through a 21-gauge needle until all muscle was broken apart. The remaining cell slurry was filtered through a 40 μM cell strainer that was prewet with 10 mL of cold myoblast media (DMEM:F12; 15% FBS, 1X anti-anti) the strainer was rinsed with an additional 10 mL of cold myoblast media, and cells were pelleted at 300x*g*/4°C. Cells were incubated with 1mL 1X red cell lysis buffer (ThermoFisher) for 5 min at room temperature and 9 mL cold FACS buffer (2.5% goat serum, 2 mM EDTA, pH 8.0 in 1X PBS) was added. Cells were spun and resuspended in 1mL of FACS buffer containing biotin-conjugated antibodies raised against antigens CD45, CD31, CD11b, and Sca1 prior to an incubation on ice for 45 min. Cells were centrifuged and resuspended in 100 μL of FACS buffer containing antibodies CD34, and α7-integrin, as well as streptavidin-PE-Cy7. Cells were incubated in the dark for 90 min on ice, with agitation occurring every 30 min. FACS buffer was added up to 1 mL final volume, and cells pelleted and resuspended in FACS buffer, and the viability dye 7-aminoactinomycin D (7-AAD) was added (final concentration 4 mg/mL). Cells were placed in falcon tubes with cell strainers before collection by FACS. Murine MuSCs were identified as $CD11b^{-}/CD31^{-}/CD45^{-}/Sca1^{-}/\alpha7\text{-}Integrin^{+}/CD34^{+}$. Primary human MuSCs were provided as described (Tichy et al., 2017). Briefly, human calf muscle biopsies were enzymatically dissociated in

0.2% collagenase (Sigma-Aldrich) and 0.02 units/mL dispase (Roche) for 45 min at 37°C, minced under a dissection microscope and incubated for an additional 45 min at 37°C. The resulting cell suspension was filtered through a 70 μm cell strainer and incubated with biotinylated anti-human CD45, CD11b and CD31. Samples were washed with FACS buffer and incubated with anti-NCAM/CD56 and Streptavidin APC-Cy7. Human MuSCs were $CD11b^{-}/CD31^{-}/CD45^{-}/NCAM^{+}$.

Flow cytometry—FACS-isolated MuSCs from age and sex-matched animals were fixed in 1.6% PFA/PBS for 10' on ice, spun at 350*xg* at 4°C, and stored in cold 100% methanol (final concentration 90%) at −80°C until the staining commenced. MuSCs were further permeabilized in 1% Igepal CA-630/PBS, washed with PBS, and blocked with 1% BSA/PBS/0.1% Triton X-100, and stained with phospho-p65 antibody (Abcam, 1/500), or phospho-JNK (1/100, Cell Signaling), phospho-p38 (1/100, BD Biosciences), phospho-S6K (1/100, Cell Signaling), phospho-AKT (1/100, Cell Signaling), or Bcl2 (1/100, BD Biosciences) in 1%BSA/PBS/0.1% Triton X-100 overnight at 4°C in V-bottom 96-well plates. MuSCs were washed in BSA buffer, stained with goat anti-mouse or goat anti-rabbit IgG Alexa Fluor 488 antibody (Thermo, 1/500), and analyzed on an LSRII flow cytometer using the 488nm laser line 530/30 bandpass filter set. Data were analyzed with FlowJo. Unbiased analysis was performed with the investigators blinded to genotypes and/or conditions. Results were consistent and reproducible with different batches of Abs, using MuSC isolation from different experimental mice performed on different days. Antibody specificity was determined by several methods, including using unstained controls, no primary antibody-stained controls, and FMO controls.

Muscle isolation and sectioning—Tibialis Anterior muscles were dissected and fixed in 4% PFA/PBS and incubated overnight in 30% sucrose prior to being embedded in OCT medium (Richard Allen Scientific) and frozen in chilled 2-methylbutane. Cryosections were cut at a thickness of 10 μm and placed on Superfrost plus slides. Sections were stained with Hematoxylin and Eosin. More specifically, slides were stained with Hematoxylin for 1min, rinsed in water, and incubated with acidic alcohol (1% hydrochloric acid in 100% ethanol). After rinsing in water, slides were immersed in bluing, water, and 70% ethanol for 30sec each. Next, slides were exposed to eosin for 1min and gradually dehydrated with a graduated ethanol series. After a final incubation in xylene, coverslips were mounted with Cytoseal-xyl. Sections were imaged on a Nikon Ni widefield epifluorescence microscope. Muscle fiber areas were manually determined using ImageJ/Fiji.

Immunofluorescence staining—Isolated cells or tissue cryosections were permeabilized in 0.5% Triton X-100/PBS for 10min and washed with PBS. If Pax7 staining was required, sections were processed as in Tichy et al. (2018). Primary antibodies for phospho-p65 (1/100; Abcam), Ki67 (1/250; Abcam) and/or 53BP1 (1/1000; Novus Biologicals) were incubated overnight at 4°C in antibody dilution buffer (1% BSA/PBS/0.1% Triton X-100). Secondary antibodies used were: Alexa Fluor 488 and Alexa Fluor 647-conjugated goat anti-mouse or anti-rabbit staining (1/300–500 in antibody dilution buffer) for 1hr in the dark at room temperature. For quantifications in Figure 1, p-p65 expression represent nuclear signal intensities normalized to DAPI intensities, to account for any

possible differences in cell cycle position or nuclear size. A negative staining control (with no primary antibody) was included to further demonstrate the specificity of the p-p65 staining. For human sections, 10um formalin-fixed paraffin-embedded skeletal muscle from young normal donors or DMD patients were deparaffinized and rehydrated by standard procedures. Samples were permeabilized with 0.5% Triton X100/PBS, underwent heat-mediated antigen retrieval with acidic citrate, and were blocked first with the avidin/biotin blocking kit (Vector Labs), then with 3% BSA/PBS/0.1% Triton X-100. Sections were stained with Ku80 antibody (Proteintech) and Pax7 (Santa Cruz) overnight at 4°C in 1% BSA/PBS/0.1% Triton X-100. Slides were washed with PBS and the Pax7 signal was amplified with a mouse-on mouse kit (Vector labs). Sections were stained with Alexa Fluor 488 Goat anti-Rabbit IgG and Alexa Fluor 647-conjugated streptavidin for 1hr. All slides washed with PBS and coverslips were mounted with prolong gold with DAPI. Sections were imaged with a Nikon Ni widefield epifluorescence microscope under the same conditions and intensities of Ku80 in Pax7 cells were normalized to controls.

Trichrome staining—For Masson's trichrome staining, tissue cryosections were fixed with Bouin's solution overnight, rinsed with water, and incubated with Weigert's Hematoxylin staining reagent (Electron Microscopy Sciences) for 5 min. Slides were washed with water for 10 min and stained with a commercially available kit (Sigma Aldrich). Briefly, slides were first stained with Biebrich Scarlet-Acid Fuchsin Solution (Sigma Aldrich) for 5 min, rinsed in three changes of water, followed by staining with phosphotungstic/phosphomolybdic acid solution (Sigma Aldrich) for 10 min. Slides were then stained with aniline blue solution (Sigma Aldrich) for 5min to stain collagen in blue, differentiated with 1% glacial acetic acid for 2min, and then dehydrated with an ascending series of ethyl alcohol followed by xylene before they were mounted. Sections were imaged under the same conditions and intensities using a Nikon Ni widefield epifluorescence microscope with an objective lens magnification at 20×. Analysis of fibrotic area was conducted in Fiji software, using color deconvolution and thresholding function to define the areas of collagen and the muscle fiber. The fibrotic area percentage is calculated as (collagen area/muscle fiber area) × 100.

Telomere length analysis of FACS isolated MuSCs (MuQ-FISH)—Telomere length was measured using quantitative fluorescent *in situ* hybridization of Cy3-conjugated PNA telomere probe (Tel-C, PNA probe). MuSCs were isolated and processed for telomere length measurements as previously described (Tichy et al., 2017). MuSCs were imaged using a Nikon eclipse 90i wide-field epifluorescence microscope equipped with a Prior Proscan III motorized stage, a Photometrics Coolsnap HQ2 14-bit digital camera and a Nikon 100x/1.40 Plan Apo VC objective. Initially, control samples are imaged to determine each channel's exposure time in a way that situates the intensities for all samples in the mid-intensity range. This control prevents overexposure or loss of signal detection with the selected exposure times during sample imaging. Once an optimal exposure time is defined, image acquisition is utilized at the same exposure settings for the telomere and DAPI or centromeric signals for imaging of individual experiments. For each experiment, the intensity settings are not changed between sample groups. Images are taken without binning. Imaging must take place in the same time window for each experiment, and combination of multiple experiments

performed at different days is not recommended, due to the inherent caveat of fluorescent intensity measurements differing between experiments. Telomere length was assessed as the total sum or mean telomeric probe intensity divided by the sum intensity of either the DAPI or the centromeric signal. Unbiased analysis with the investigators blinded to genotypes and/or conditions was conducted using the ImageJ plug-in Telometer.

Telomere length analysis of tissues sections—PFA-fixed cryosections were permeabilized for 10min with 0.5% Triton X-100, washed with PBS, and underwent heat-mediated antigen retrieval with TET buffer (10mM Tris, pH 7.5, 1mM EDTA, pH 8.0, 0.05% Tween-20). Sections were incubated with Tel C-Alexa Fluor 647 and CENPB-Cy3 (PNA bio, 1/600) in QFISH cryo-buffer (15% ethylene carbonate, 20% dextran sulfate, 600mM NaCl, 0.1% citric acid-based antigen retrieval buffer). Probe in buffer was added to slides, covered with a coverslip, and QFISH was carried out using a Thermobrite programmable slide warmer (Leica): 10min prehybridization step at 67°C, followed by 90min hybridization at 42C. Afterward, slides were washed twice, 5min each in buffers with decreasing salt concentrations at 55°C (2X SSC/0.1% Tween 20, 1X SSC/0.1% Tween 20, 0.5X SSC/0.1% Tween 20, 0.25X SSC/0.1% Tween 20). Slides were rinsed with PBS, blocked with 1% BSA/0.1% Triton X-100/1X PBS for 1hr at room temperature. Antibody to VCAM (ThermoFisher, 1/100) was added to the blocking buffer and slides were incubated overnight at 4°C. The following day, slides were washed with PBS and stained with Alexa Fluor 488-conjugated Donkey anti-goat IgG antibody (ThermoFisher) in blocking buffer for 1hr at room temperature. Slides were washed with PBS and coverslips were mounted with Prolong gold plus DAPI. Cryosections were imaged with a Nikon Ni widefield epifluorescence microscope equipped with a 100x Plan Apo objective and Nikon elements software. Analysis of telomere length was assessed with the investigators blinded to genotypes and/or conditions in $VCAM^+$ cells using Telometer. At least 40 cells per mouse were analyzed.

MuSC proliferation assays—Mice were injected with EdU (100mg/kg) IP, following the experimental design shown in Figure 3. MuSCs were plated overnight following sorting on laminin-coated 8-well chamber slides (~2500 cells) in DMEM/F12 supplemented with 15% FBS, 1X antibiotic/antimycotic, 1X Glutamax, 1X NEAA. Cells were fixed the following day in 3.7% formaldehyde/PBS for 15min and processed for EdU incorporation using the Click-iT EdU Alexa Fluor 594 Imaging kit (ThermoFisher), according to the manufacturer's instructions.

Grip test—Mice were inverted on a cross-hatched metal platform and the time required for mice to release themselves from the platform was quantified. Three repetition measurements were recorded per mouse, giving the mouse 1hr rest in between measurements.

Creatine kinase assay—Blood was collected from mice by cardiac puncture and allowed to clot. After centrifugation for 10min at 600 $\times g$, serum was diluted 1/10 with PBS and assayed and analyzed using a commercially available kit (Sekisui Diagnostics) according to the manufacturer's instructions.

Quantitative real time-PCR (qRT-PCR)—RNA was isolated from FACS-sorted MuSCs using a RNeasy Plus micro kit (QIAGEN), according to the manufacturer's instructions. cDNA was generated with the Protoscript II First Strand cDNA synthesis kit (New England Biolabs). qRT-PCR was carried out on a Quantstudio 6 instrument (Applied Biosystems) using Taqman primers and Taqman Universal PCR Master Mix. Reactions were carried out in triplicate with at least three mice analyzed per experiment. Gene expression was determined using the ΔΔCt method. Primers purchased from Applied Biosystems and included IKBKB-FAM (Gene assay ID: Mm01222247_m1), CHUK-FAM (Mm00432529_m1), IKBKG-FAM (Mm00494927_m1), XRCC5-FAM (Mm00550142_m1), XRCC6-FAM (Mm00487458_m1), TERF2-FAM (Mm01253555_m1), TERF1-FAM (Mm00436928_m1), TERF2IP-FAM (Mm01243676_m1), TPP1-FAM (Mm00487016_m1), TINF2-FAM (Mm00461166_g1), Pot1B-FAM (Mm01278790_m1), Tert-FAM (Mm00436931_m1), and GAPDH-VIC (4352339e).

***In silico* analysis of putative p65 binding sites in promoters—**The potential of the p65 transcription factor to bind to selected murine gene promoters was analyzed using the Lasagna tool (https://biogrid.engr.uconn.edu/lasagna_search/) with the following conditions: using the transfac model, search range of −2000 to 0, p less than or equal to 0.001. Displayed are the

Telomere-induced foci (TIF) assay—For chronic injury assessment, mice were injured in the Tibialis Anterior muscle with 10uL of 10ug/mL notexin weekly, for three times and harvested 3 days after the last injury. For dystrophic models, mice were injured once and harvested 3 days post-injury. 10 μm cryosections were stained as described in "telomere length analysis in tissue sections" above using a Tel-C Alexa Fluor 647-conjugated probe (PNA bio). After staining and processing, slides were blocked for 2 hours at room temperature with 3% BSA in PBS, followed by overnight incubation at 4°C with antibody to VCAM (1/100 of 1 μg/μL stock ThermoFisher) and 53BP1 (1/2000, Novus Biologicals). Slides were rinsed in PBS and incubated with donkey anti-goat Alexa fluor-conjugated secondary antibodies (1/300) for 1 hour at room temperature. Slides were washed with PBS three times before mounting coverslips with prolong gold with DAPI. For imaging, 1 μm slices were captured with a Zeiss Confocal 710 microscope with Zen software. TIFs were defined as 53BP1 foci overlapping or contacting telomere foci. For TIF assessment of human-derived MuSCs, cells were plated on collagen-coated chamber slides and stained with TelC-Alexa 647 PNA probe (according to Telomere Length Analysis of FACS Isolated MuSCs (MuQ-FISH) above). Slides were blocked with 3% BSA in PBS for 1 hour and stained with 53BP1 antibody (1/2000) overnight at 4°C, followed by staining with Alexa Fluor 488-conjugated secondary antibody for 1 hour at room temperature. Coverslips were mounted with fluoromount G with DAPI (Southern Biotech). Cells were imaged on a Nikon widefield epifluorescence microscope and quantitated for TIFs.

In-cell western—Human-derived MuSCs were plated in collagen-coated 96-well optical bottom plates in equal numbers, fixed in 4% PFA/PBS, permeabilized with 1% IGEPAL CA-630, blocked in 10% goat serum/1% BSA/PBS and stained with antibody against phospho-p65 serine 536 (1/100; Abcam) overnight at 4°C. Cells were washed with PBS and

stained with Dylight 800 goat anti-rabbit (1/1,000; Rockland) and DNA was stained with DRAQ5 (1/5,000; Biolegend). Signal intensities were measured on an Odyssey Infrared Imaging System, with Image Studio software. Antibody intensity to nuclear intensity ratios were analyzed to normalize for cell content/growth differences.

Imaging using two-photon microscopy—To define MuSC number in their endogenous environment, Control (Pax7EGFP) and genetically modified mice bred to Pax7EGFP mice were injured 3X with notexin, starting around 3 months of age, and allowed to recover for ~10 weeks. TA muscles were collected, fixed in 4% PFA/PBS and rinsed in PBS. Muscles were mounted on a custom-made chamber and high-resolution serial sections were collected from the middle of the muscle, using a Leica SP* Confocal/Multiphoton Microscope system equipped with a Chameleon Vision II Sapphire laser. A 910 nm laser was focused through a 20x HCX APO L Lens. Emission light was collected with a FITC (BP 525/50) filter, and muscle fibers were marked via second-generation harmonics. Serial optical sections were collected every 1.5 μm, flattened, and normalized to volume scanned.

uCT imaging—Each mouse was scanned *in vivo* using a preclinical μCT system (vivaCT 40, Scanco Medical AG, Brüttisellen, Switzerland) at 38μm nominal voxel size. The scanner was used at 55kVp energy and 145μA intensity. Images were generated with an integration time of 200ms and 1 signal average. During the scans, mice were anesthetized using 1%–1.5% isoflurane in 1–1.5mL/min of oxygen. The mouse was immobilized using a customized holder to ensure minimal motion. Before each scan, a 2D scout view was used to select the scan region. The average scan time was approximately 50min.

Myoblast culture and shRNA knockdown—C2C12 myoblast cells were grown in DMEM high glucose supplemented with 10% fetal bovine serum, 1X antibiotic/antimycotic, 1X Glutamax, and 1X nonessential amino acids. Equal numbers of cells were plated at low density (3×10^4 cells/well) into 24 well plates and transfected with shRNA vectors using lipofectamine 3000, according to the manufacturer's instructions. Vectors used were shEMPTY (pLKO1.puro empty; Addgene plasmid 8453), mouse XRCC5–1 (Sigma SHCLNG-NM_009533; TRCN000031295), mouse XRCC5–2 (Sigma SHCLNG-NM_009533; TRCN0000071044). Transfected cells were re-plated in 8 well chamber slides 24 hours post-transfection, cultured a further 24 hours, and either subjected to MuQ-FISH or stained with antibody to Ku80 (Santa Cruz, B4, Alexa Fluor 647-conjugated) and imaged. Data were generated from 3 independently transfected wells which were stained, imaged and analyzed at the same end points. Analysis of nuclear Ku80 expression was determined using a semi-automated protocol in ImageJ.

Functional measurements—Muscle contractility was tested at the Penn Muscle Institute Muscle Physiology Assessment Core of the University of Pennsylvania. Eccentrics (ECCs) were assessed on freshly isolated EDL muscles using an Aurora Mouse 1200A System equipped with Dynamic Muscle Control v.5.5 software. EDL muscles were maintained in constantly oxygenated Ringer's solution (100mM NaCl, 4.7mM KCl, 3.4mM $CaCl_2$, 1.2mM KH_2PO_4, 1.2mM $MgSO_4$, 25mM HEPES and 5.5mM D-glucose) at 24 C. Briefly, a series of two ECCs was applied using a tetanic stimulation of 80Hz and stretching

the muscle by 10% of L0 over 200ms. The force drop was calculated as the percent of the force at the initial ECC.

QUANTIFICATION AND STATISTICAL ANALYSIS

Dataset values are described in the figure legends and are presented as mean ± SEM (standard error of the mean). n = number of mice per genotype. n = numbers of cells analyzed per mouse. Specific details on mouse numbers, age and statistics can be found in the figure legends. Analyses were performed using GraphPad Prism 6 software. *$p \leq 0.05$; **$p \leq 0.01$, *** $p < 0.001$, **** $p < 0.0001$. All investigators were blinded when analyzing data.

Supplementary Material

Refer to Web version on PubMed Central for supplementary material.

ACKNOWLEDGMENTS

We thank A. Sacco for providing the human samples, M. Pasparakis for providing the NEMO$^{fl/fl}$ mice, and W.J. Tseng and S. Liu (PCMD Imaging Core) for assistance with the μCT experiments. We would like to thank H. Papaioannou, A. Scaramella, I. Paez, Y. Lee, and G. Wang for unbiased validation and analysis assistance. The authors were supported by startup funds from the Perelman School of Medicine, the McCabe Award, the NIH Pilot Grant (P30 AR069619), NASA (18-FG_ind_2-0022), and the NIH (R01HL146662) to F.M.

REFERENCES

Acharyya S, Villalta SA, Bakkar N, Bupha-Intr T, Janssen PM, Carathers M, Li ZW, Beg AA, Ghosh S, Sahenk Z, et al. (2007). Interplay of IKK/NF-kappaB signaling in macrophages and myofibers promotes muscle degeneration in Duchenne muscular dystrophy. J. Clin. Invest. 117, 889–901. [PubMed: 17380205]

Baghdiguian S, Martin M, Richard I, Pons F, Astier C, Bourg N, Hay RT, Chemaly R, Halaby G, Loiselet J, et al. (1999). Calpain 3 deficiency is associated with myonuclear apoptosis and profound perturbation of the IkappaB alpha/NF-kappaB pathway in limb-girdle muscular dystrophy type 2A. Nat. Med. 5, 503–511. [PubMed: 10229226]

Boldrin L, Zammit PS, and Morgan JE (2015). Satellite cells from dystrophic muscle retain regenerative capacity. Stem Cell Res. (Amst.) 14, 20–29.

Boulton SJ, and Jackson SP (1998). Components of the Ku-dependent non-homologous end-joining pathway are involved in telomeric length maintenance and telomeric silencing. EMBO J. 17, 1819–1828. [PubMed: 9501103]

Cai D, Frantz JD, Tawa NE Jr., Melendez PA, Oh BC, Lidov HG, Hasselgren PO, Frontera WR, Lee J, Glass DJ, and Shoelson SE (2004). IKKbeta/NF-kappaB activation causes severe muscle wasting in mice. Cell 119, 285–298. [PubMed: 15479644]

Calado DP, Zhang B, Srinivasan L, Sasaki Y, Seagal J, Unitt C, Rodig S, Kutok J, Tarakhovsky A, Schmidt-Supprian M, and Rajewsky K (2010). Constitutive canonical NF-κB activation cooperates with disruption of BLIMP1 in the pathogenesis of activated B cell-like diffuse large cell lymphoma. Cancer Cell 18, 580–589. [PubMed: 21156282]

Chai W, Ford LP, Lenertz L, Wright WE, and Shay JW (2002). Human Ku70/80 associates physically with telomerase through interaction with hTERT. J. Biol. Chem. 277, 47242–47247. [PubMed: 12377759]

Chazaud B, Sonnet C, Lafuste P, Bassez G, Rimaniol AC, Poron F, Authier FJ, Dreyfus PA, and Gherardi RK (2003). Satellite cells attract monocytes and use macrophages as a support to escape apoptosis and enhance muscle growth. J. Cell Biol. 163, 1133–1143. [PubMed: 14662751]

d'Adda di Fagagna F, Hande MP, Tong WM, Roth D, Lansdorp PM, Wang ZQ, and Jackson SP (2001). Effects of DNA nonhomologous end-joining factors on telomere length and chromosomal stability in mammalian cells. Curr. Biol. 11, 1192–1196. [PubMed: 11516951]

de Lange T (2005). Shelterin: the protein complex that shapes and safeguards human telomeres. Genes Dev. 19, 2100–2110. [PubMed: 16166375]

Didier N, Hourdé C, Amthor H, Marazzi G, and Sassoon D (2012). Loss of a single allele for Ku80 leads to progenitor dysfunction and accelerated aging in skeletal muscle. EMBO Mol. Med. 4, 910–923. [PubMed: 22915554]

Dong J, Jimi E, Zhong H, Hayden MS, and Ghosh S (2008). Repression of gene expression by unphosphorylated NF-kappaB p65 through epigenetic mechanisms. Genes Dev. 22, 1159–1173. [PubMed: 18408078]

Dumont NA, Wang YX, von Maltzahn J, Pasut A, Bentzinger CF, Brun CE, and Rudnicki MA (2015). Dystrophin expression in muscle stem cells regulates their polarity and asymmetric division. Nat. Med. 21, 1455–1463. [PubMed: 26569381]

Emery AE (2002). Muscular dystrophy into the new millennium. Neuromuscul. Disord. 12, 343–349. [PubMed: 12062251]

Espejel S, Klatt P, Ménissier-de Murcia J, Martín-Caballero J, Flores JM, Taccioli G, de Murcia G, and Blasco MA (2004). Impact of telomerase ablation on organismal viability, aging, and tumorigenesis in mice lacking the DNA repair proteins PARP-1, Ku86, or DNA-PKcs. J. Cell Biol. 167, 627–638. [PubMed: 15545322]

Fell VL, and Schild-Poulter C (2015). The Ku heterodimer: function in DNA repair and beyond. Mutat. Res. Rev. Mutat. Res. 763, 15–29. [PubMed: 25795113]

Frenette J, Cai B, and Tidball JG (2000). Complement activation promotes muscle inflammation during modified muscle use. Am. J. Pathol. 156, 2103–2110. [PubMed: 10854231]

Gallego ME, Jalut N, and White CI (2003). Telomerase dependence of telomere lengthening in Ku80 mutant Arabidopsis. Plant Cell 15, 782–789. [PubMed: 12615949]

Hammers DW, Sleeper MM, Forbes SC, Coker CC, Jirousek MR, Zimmer M, Walter GA, and Sweeney HL (2016). Disease-modifying effects of orally bioavailable NF-κB inhibitors in dystrophin-deficient muscle. JCI Insight 1, e90341. [PubMed: 28018975]

Hayden MS, and Ghosh S (2004). Signaling to NF-kappaB. Genes Dev. 18, 2195–2224. [PubMed: 15371334]

He WA, Berardi E, Cardillo VM, Acharyya S, Aulino P, Thomas-Ahner J, Wang J, Bloomston M, Muscarella P, Nau P, et al. (2013). NF-κB-mediated Pax7 dysregulation in the muscle microenvironment promotes cancer cachexia. J. Clin. Invest. 123, 4821–4835. [PubMed: 24084740]

Hoffman EP, Brown RH Jr., and Kunkel LM (1987). Dystrophin: the protein product of the Duchenne muscular dystrophy locus. Cell 51, 919–928. [PubMed: 3319190]

Hsu HL, Gilley D, Blackburn EH, and Chen DJ (1999). Ku is associated with the telomere in mammals. Proc. Natl. Acad. Sci. USA 96, 12454–12458. [PubMed: 10535943]

Hsu HL, Gilley D, Galande SA, Hande MP, Allen B, Kim SH, Li GC, Campisi J, Kohwi-Shigematsu T, and Chen DJ (2000). Ku acts in a unique way at the mammalian telomere to prevent end joining. Genes Dev. 14, 2807–2812. [PubMed: 11090128]

Im WB, Phelps SF, Copen EH, Adams EG, Slightom JL, and Chamberlain JS (1996). Differential expression of dystrophin isoforms in strains of mdx mice with different mutations. Hum. Mol. Genet. 5, 1149–1153. [PubMed: 8842734]

Indiviglio SM, and Bertuch AA (2009). Ku's essential role in keeping telomeres intact. Proc. Natl. Acad. Sci. USA 106, 12217–12218. [PubMed: 19622731]

Jurk D, Wilson C, Passos JF, Oakley F, Correia-Melo C, Greaves L, Saretzki G, Fox C, Lawless C, Anderson R, et al. (2014). Chronic inflammation induces telomere dysfunction and accelerates ageing in mice. Nat. Commun. 2, 4172. [PubMed: 24960204]

Koike M, and Koike A (2008). Accumulation of Ku80 proteins at DNA double-strand breaks in living cells. Exp. Cell Res. 314, 1061–1070. [PubMed: 18164703]

Kottlors M, and Kirschner J (2010). Elevated satellite cell number in Duchenne muscular dystrophy. Cell Tissue Res. 340, 541–548. [PubMed: 20467789]

Lee HW, Blasco MA, Gottlieb GJ, Horner JW 2nd, Greider CW, and DePinho RA (1998). Essential role of mouse telomerase in highly proliferative organs. Nature 392, 569–574. [PubMed: 9560153]

Li H, Vogel H, Holcomb VB, Gu Y, and Hasty P (2007). Deletion of Ku70, Ku80, or both causes early aging without substantially increased cancer. Mol. Cell. Biol. 27, 8205–8214. [PubMed: 17875923]

Mao Z, Bozzella M, Seluanov A, and Gorbunova V (2008). Comparison of nonhomologous end joining and homologous recombination in human cells. DNA Repair (Amst.) 7, 1765–1771. [PubMed: 18675941]

Melnikova L, Biessmann H, and Georgiev P (2005). The Ku protein complex is involved in length regulation of Drosophila telomeres. Genetics 170, 221–235. [PubMed: 15781709]

Messina S, Vita GL, Aguennouz M, Sframeli M, Romeo S, Rodolico C, and Vita G (2011). Activation of NF-kappaB pathway in Duchenne muscular dystrophy: relation to age. Acta Myol. 30, 16–23. [PubMed: 21842588]

Morgan JE, and Zammit PS (2010). Direct effects of the pathogenic mutation on satellite cell function in muscular dystrophy. Exp. Cell Res. 316, 3100–3108. [PubMed: 20546725]

Mourkioti F, and Rosenthal N (2008). NF-kappaB signaling in skeletal muscle: prospects for intervention in muscle diseases. J. Mol. Med. (Berl.) 86, 747–759. [PubMed: 18246321]

Mourkioti F, Kratsios P, Luedde T, Song YH, Delafontaine P, Adami R, Parente V, Bottinelli R, Pasparakis M, and Rosenthal N (2006). Targeted ablation of IKK2 improves skeletal muscle strength, maintains mass, and promotes regeneration. J. Clin. Invest. 116, 2945–2954. [PubMed: 17080195]

Mourkioti F, Kustan J, Kraft P, Day JW, Zhao MM, Kost-Alimova M, Protopopov A, DePinho RA, Bernstein D, Meeker AK, and Blau HM (2013). Role of telomere dysfunction in cardiac failure in Duchenne muscular dystrophy. Nat. Cell Biol. 15, 895–904. [PubMed: 23831727]

Murphy MM, Lawson JA, Mathew SJ, Hutcheson DA, and Kardon G (2011). Satellite cells, connective tissue fibroblasts and their interactions are crucial for muscle regeneration. Development 138, 3625–3637. [PubMed: 21828091]

Oda T, Shimizu N, Yonenobu K, Ono K, Nabeshima T, and Kyoh S (1993). Longitudinal study of spinal deformity in Duchenne muscular dystrophy. J. Pediatr. Orthop. 13, 478–488. [PubMed: 8370781]

Oh J, Sinha I, Tan KY, Rosner B, Dreyfuss JM, Gjata O, Tran P, Shoelson SE, and Wagers AJ (2016). Age-associated NF-κB signaling in myofibers alters the satellite cell niche and re-strains muscle stem cell function. Aging (Albany NY) 8, 2871–2896. [PubMed: 27852976]

Proto JD, Lu A, Dorronsoro A, Scibetta A, Robbins PD, Niedernhofer LJ, and Huard J (2017). Inhibition of NF-κB improves the stress resistance and myogenic differentiation of MDSPCs isolated from naturally aged mice. PLoS ONE 12, e0179270. [PubMed: 28640861]

Sacco A, Mourkioti F, Tran R, Choi J, Llewellyn M, Kraft P, Shkreli M, Delp S, Pomerantz JH, Artandi SE, and Blau HM (2010). Short telomeres and stem cell exhaustion model Duchenne muscular dystrophy in mdx/mTR mice. Cell 143, 1059–1071. [PubMed: 21145579]

Sasaki Y, Derudder E, Hobeika E, Pelanda R, Reth M, Rajewsky K, and Schmidt-Supprian M (2006). Canonical NF-kappaB activity, dispensable for B cell development, replaces BAFF-receptor signals and promotes B cell proliferation upon activation. Immunity 24, 729–739. [PubMed: 16782029]

Schmidt-Supprian M, Bloch W, Courtois G, Addicks K, Israë l A, Rajewsky K, and Pasparakis M (2000). NEMO/IKK gamma-deficient mice model incontinentia pigmenti. Mol. Cell 5, 981–992. [PubMed: 10911992]

Takai H, Smogorzewska A, and de Lange T (2003). DNA damage foci at dysfunctional telomeres. Curr. Biol. 13, 1549–1556. [PubMed: 12956959]

Teo H, Ghosh S, Luesch H, Ghosh A, Wong ET, Malik N, Orth A, de Jesus P, Perry AS, Oliver JD, et al. (2010). Telomere-independent Rap1 is an IKK adaptor and regulates NF-kappaB-dependent gene expression. Nat. Cell Biol. 12, 758–767. [PubMed: 20622870]

Tichy ED, Sidibe DK, Tierney MT, Stec MJ, Sharifi-Sanjani M, Hosalkar H, Mubarak S, Johnson FB, Sacco A, and Mourkioti F (2017). Single Stem Cell Imaging and Analysis Reveals Telomere

Length Differences in Diseased Human and Mouse Skeletal Muscles. Stem Cell Reports 9, 1328–1341. [PubMed: 28890163]

Tichy ED, Sidibe DK, Greer CD, Oyster NM, Rompolas P, Rosenthal NA, Blau HM, and Mourkioti F (2018). A robust Pax7EGFP mouse that enables the visualization of dynamic behaviors of muscle stem cells. Skelet. Muscle 8, 27. [PubMed: 30139374]

Tidball JG (2005). Inflammatory processes in muscle injury and repair. Am. J. Physiol. Regul. Integr. Comp. Physiol 288, R345–R353. [PubMed: 15637171]

Tidball JG, and Wehling-Henricks M (2015). Shifts in macrophage cytokine production drive muscle fibrosis. Nat. Med. 21, 665–666. [PubMed: 26151325]

Wilkins KE, and Gibson DA (1976). The patterns of spinal deformity in Duchenne muscular dystrophy. J. Bone Joint Surg. Am. 58, 24–32. [PubMed: 1249109]

Yin L, Hubbard AK, and Giardina C (2000). NF-kappa B regulates transcription of the mouse telomerase catalytic subunit. J. Biol. Chem. 275, 36671–36675. [PubMed: 10970902]

Zatz M, Rapaport D, Vainzof M, Passos-Bueno MR, Bortolini ER, Pavanello, Rde C, and Peres CA (1991). Serum creatine-kinase (CK) and pyruvate-kinase (PK) activities in Duchenne (DMD) as compared with Becker (BMD) muscular dystrophy. J. Neurol. Sci. 102, 190–196. [PubMed: 2072118]

Zhu C, Bogue MA, Lim DS, Hasty P, and Roth DB (1996). Ku86-deficient mice exhibit severe combined immunodeficiency and defective processing of V(D)J recombination intermediates. Cell 86, 379–389. [PubMed: 8756720]

Zuo QP, Liu SK, Li ZJ, Li B, Zhou YL, Guo R, and Huang LH (2011). NF-kappaB p65 modulates the telomerase reverse transcriptase in the $HepG_2$ hepatoma cell line. Eur. J. Pharmacol. 672, 113–120. [PubMed: 22008847]

Highlights

- NF-κB is dysregulated in MuSCs of dystrophic mice and DMD patients
- Persistent NF-κB activation in MuSCs leads to telomere shortening
- Unrestrained NF-κB signaling in MuSCs does not alter proliferation
- NF-κB activation in MuSCs in chronic injuries leads to Ku80 dysregulation

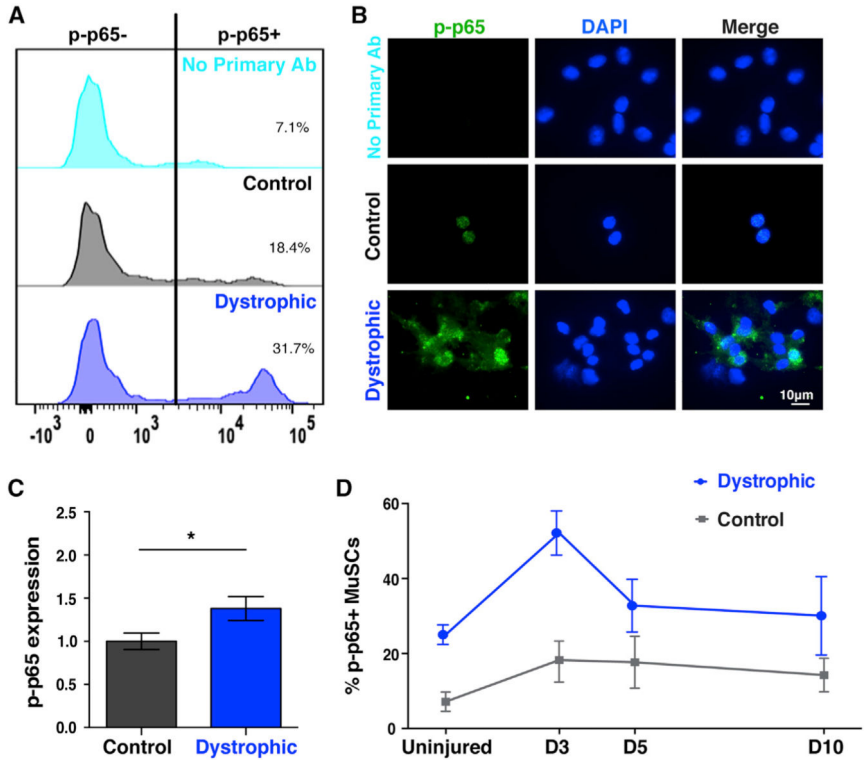

Figure 1. NF-κB activation in dystrophic MuSCs

(A) Higher NF-κB activation in FACS-isolated MuSCs from dystrophic mice, as shown by elevated phospho-p65 levels. n ≥ 3 mice (2–3 months old)/group. Percent of cells positive for p-p65 are displayed.

(B) Freshly isolated, cytospun dystrophic MuSCs exhibit accumulation of phospho-p65 compared to control MuSCs. Note the lack of staining in the no primary Ab (technical control), highlighting the specificity of the staining.

(C) Quantification shows higher levels of p-p65 in dystrophic MuSCs. n = 3 mice (2–3 months old) per genotype. n > 50 cells per condition.

(D) MuSCs from notexin-injured muscles were isolated at the indicated times. Phospho-p65+ MuSCs from dystrophic animals were elevated at all time points, including baseline conditions. n = 3 mice (3 months old)/condition. n > 1,000 cells per condition. Displayed is mean ± SEM for all graphs. Statistical analyses were performed using unpaired Student's t test with Welch's correction. *p ≤ 0.05.

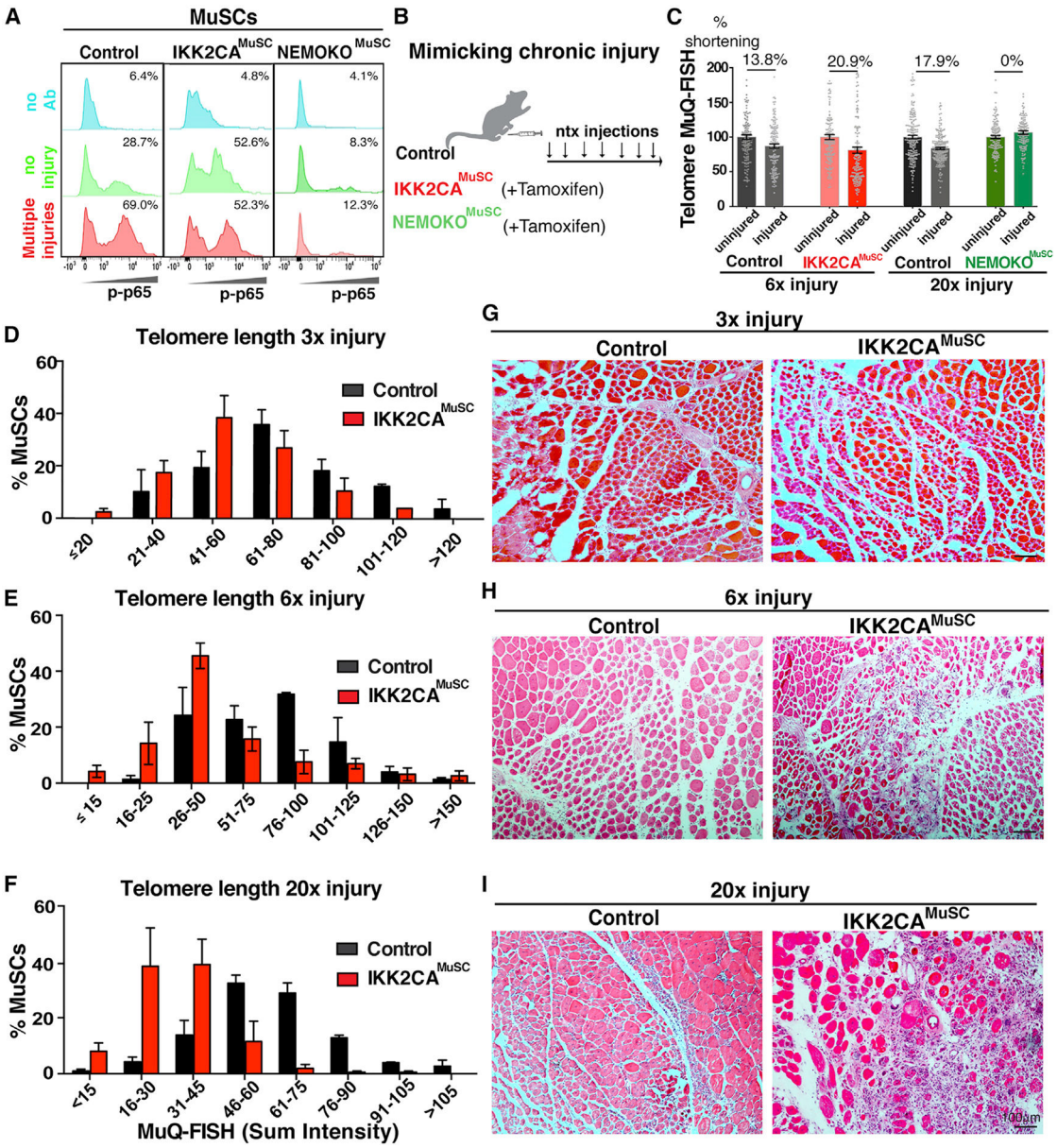

Figure 2. Persistent NF-κB activation in MuSCs leads to rapid telomere shortening

(A) p65 activation in uninjured (green plots) or injured (red plots) control MuSCs (first column), MuSCs with kinase CA of the IKK2 protein (IKK2CA^{MuSC}, second column), or MuSCs with inactivation of the NEMO protein (NEMOKO^{MuSC}, third column). Blue plots are technical controls with no primary antibody. Percent of cells positive for p-p65 is displayed.

(B) Experimental scheme for weekly notexin injuries to mimic chronic injury.

(C) IKK2CA-derived MuSCs had much shorter telomere lengths after 6× injury, while inhibition of NF-κB (NEMOKO^{MuSC}) maintains telomere length even after 20× injuries. Telomere length in MuSCs was normalized to telomere length of contralateral legs. n = 3–5 mice/genotype. Percent difference was calculated between normalized means.

(D–F) Distribution of telomere lengths of MuSCs following 3× (D), 6× (E), or 20× (F) injuries. Telomeres start to shorten after three injuries in IKK2CA^{MuSC} cells (red bars), but this reduction becomes more severe with increasing number of injuries. n = 3 mice/condition. n > 100 cells. Mean ± SEM for each bin is displayed.

(G–I) Progressive MuSC-specific telomere shortening is associated with worsened histology in IKK2CA^{MuSC} muscles at 3× (G), 6× (H), or 20× (I) injuries. n = 3–6 mice/condition. Mice were 2 months old at the time of the first injury.

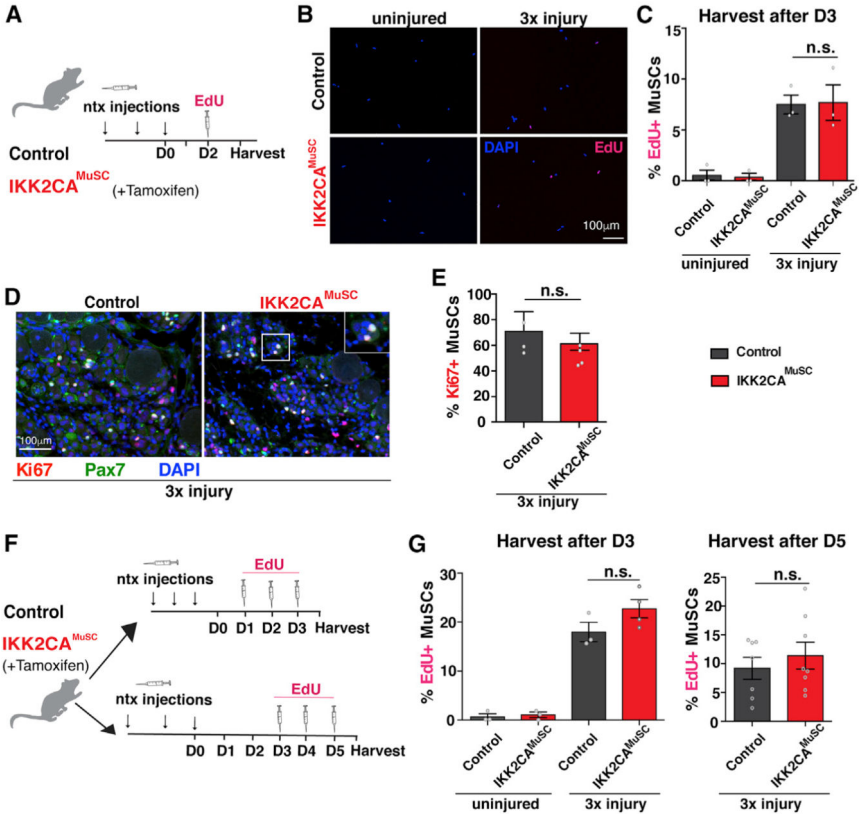

Figure 3. Activation of NF-κB does not alter *in vivo* proliferation in MuSCs under injury conditions

(A) Experimental scheme for *in vivo* 5-Ethynyl-2′deoxyuridine (EdU) incorporation assay. Mice were left uninjured or injured with notexin three times (once/week) and treated with EdU once intraperitoneally 2 days post-final injury. MuSCs were FACS-isolated 3 days post-final injury.

(B) Representative images of isolated MuSCs stained for EdU (red) and counterstained with 4’,6-diamidino-2-phenylindole (DAPI, blue).

(C) EdU quantification shows no changes in proliferation between genotypes. n = 3 mice/condition. n > 50 cells per mouse.

(D) Representative sections stained for Ki67 (red), Pax7 (green), and nuclei (DAPI, blue).

(E) Quantifications of Ki67+ MuSCs show similar proportions of proliferating MuSCs between control and IKK2CA^{MuSC} muscles. n = 3 mice/condition. n > 80 cells per mouse.

(F) Experimental schemes of additional EdU injections. Top: control and IKK2CA^{MuSC} mice injured with notexin 3× (once/week), followed by three daily EdU injections, and MuSC isolation on day 3 post-last injury (D3). Bottom: mice were notexin injured as above, followed by three daily EdU injections, and MuSC isolation on day 5 post-last injury (D5).

(G) Quantitation of EdU incorporation in MuSC-derived mice following either the D3 (left) or D5 (right) protocol. n = 3 mice (2–3 months old)/condition. n > 50 cells per mouse. No significant increases in proliferation were found in MuSCs from IKK2CA^{MuSC} compared to control mice. Data from all graphs are depicted as mean ± SEM. All statistical analyses were performed using unpaired Student’s t test with Welch’s correction. n.s., non-significant.

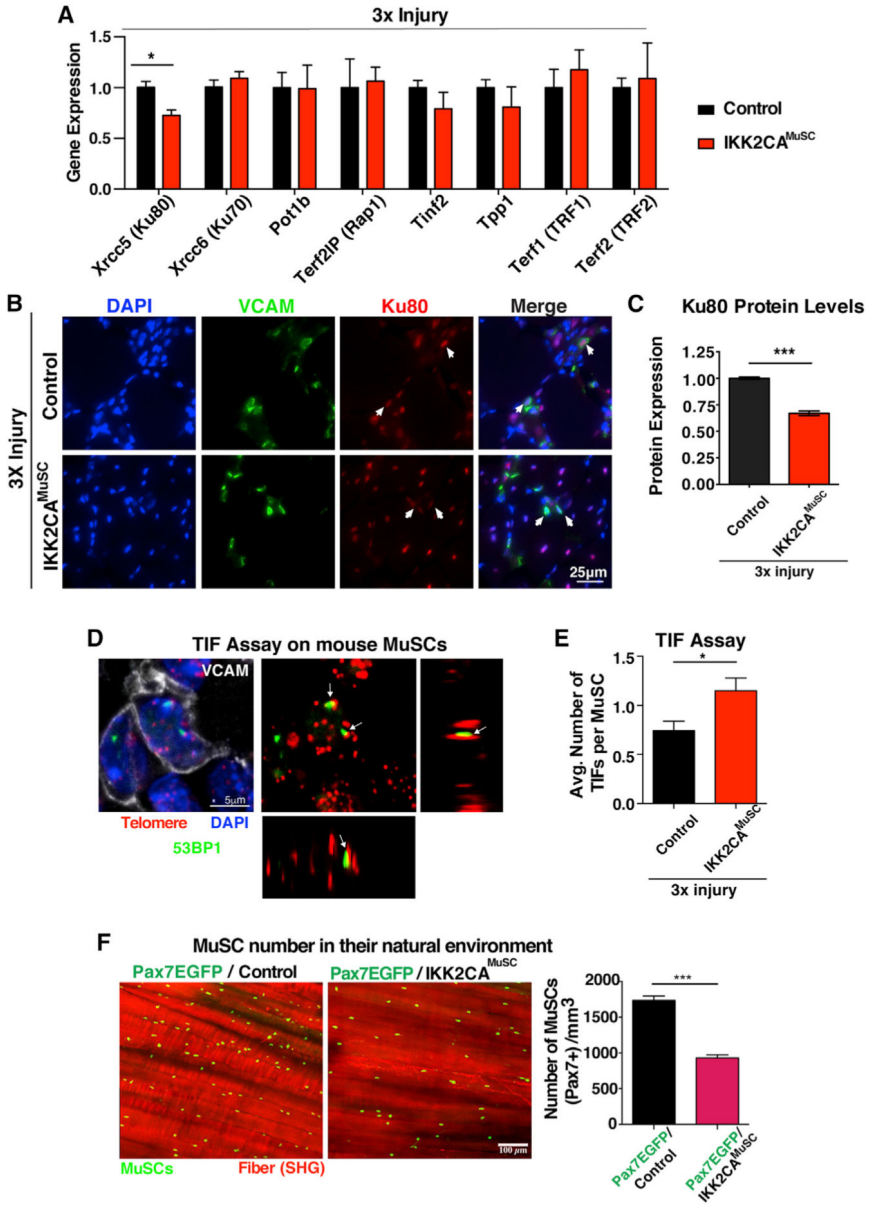

Figure 4. Activation of NF-κB in MuSCs in the context of repetitive injuries leads to Ku80 dysregulation

(A) Isolated MuSCs from 3× injured control and IKK2CA^{MuSC} mice subjected to qRT-PCR for genes associated with telomeric function. Note that *XRCC5*, which encodes the DNA repair protein, Ku80, is downregulated in IKK2CA^{MuSC} MuSCs. n = 4–7 mice (3–5 months old) per genotype.

(B) Representative Ku80 staining (red), VCAM (green), and nuclei (DAPI, blue) in muscle sections from control and IKK2CA^{MuSC} mice after 3× injury.

(C) Quantification shows reduced levels of Ku80 in IKK2CA^{MuSC} MuSCs compared to controls. n = 3 samples/group. Mean ± SEM. Statistical analysis was performed using unpaired Student's t test with Welch's correction. ***p ≤ 0.001.

(D) Representative image of TIFs (telomere-induced foci), where DNA damage (53BP1, green) co-localize with telomere (red) in VCAM-positive cells (white).
(E) Quantification shows higher TIFs in IKK2CA-^{MuSC} compared to controls. n = 3 mice (4 months old) per genotype. n > 50 cells per mouse.
(F) Left: representative two-photon microscopy images. MuSCs are shown in green, while muscle fibers are visualized in red by second harmonic generation (SHG). Right: quantification of the number of Pax7 (EGFP+) MuSCs shows stem cell exhaustion over time under chronic injuries. n = 3 mice per genotype. All datasets displayed are mean ± SEM. Statistical analyses were performed using unpaired Student's t test with Welch's correction. *$p \leq 0.05$; ***$p \leq 0.001$.

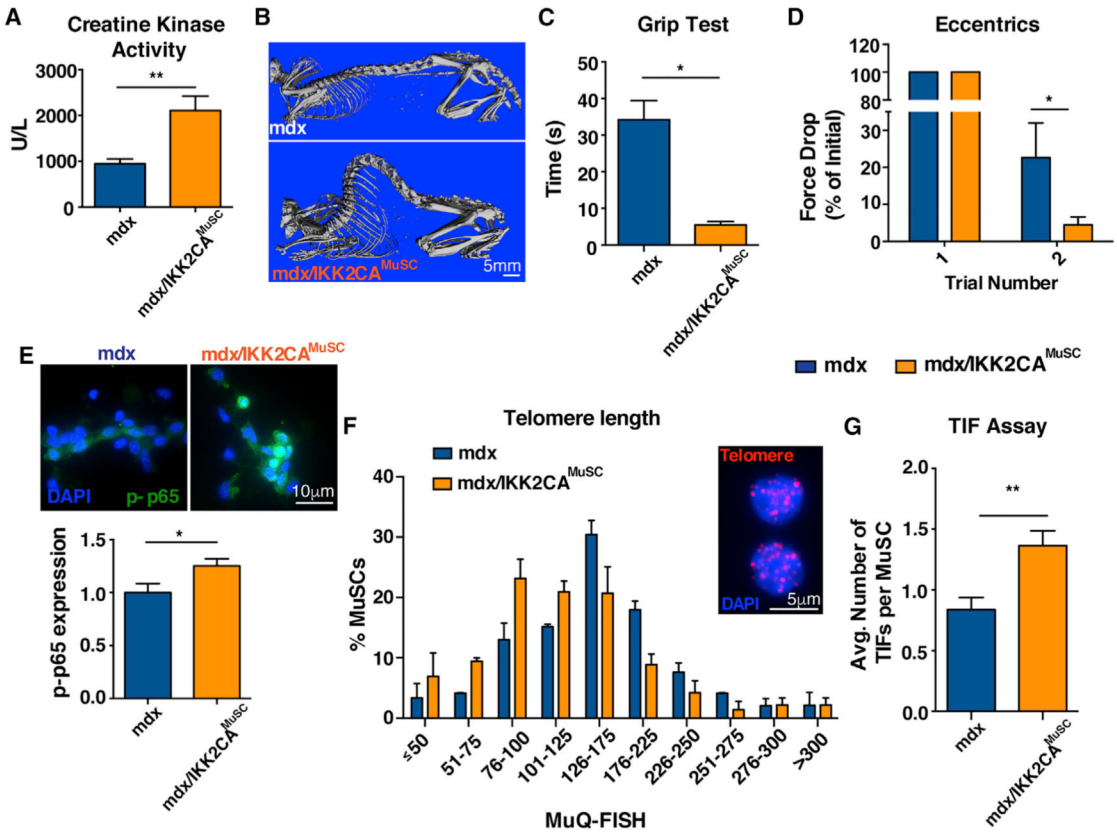

Figure 5. Activation of NF-κB in MuSCs exacerbates the mdx phenotype

To explore whether MuSC-specific activation of NF-κB could exacerbate the progression of dystrophy, mdx mice were bred to IKK2CA^{MuSC} mice, and different metrics were assessed.

(A) mdx/IKK2CA^{MuSC} exhibited more muscle damage as shown by higher serum creatine kinase activity, a strong indicator of skeletal muscle damage. n > 10 mice (8–12 months old) per genotype.

(B) Increased skeletal deformity (kyphosis), as shown by whole body CT images. n = 3–4 mice (12 months old) per genotype.

(C) mdx/IKK2CA^{MuSC} mice were substantially impaired in the grip test. n = 4–5 mice (8–12 months old) per genotype.

(D) Reduced strength of mdx/IKK2CA^{MuSC} mice compared to mdx mice. n = 3–5 mice (8–12 months old) per genotype.

(E) Higher levels of phospho-p65 in isolated MuSCs (upper) and quantification of p-p65 (lower). n = 3–4 mice (4–5 months old) per genotype. n > 30 cells per condition.

(F) Telomere length assessment by MuQ-FISH in isolated MuSCs (insert: representative image of telomere staining) shows reduced telomere length in mdx/IKK2CA^{MuSC} mice. n = 3–4 mice (5 months old) per genotype. n > 70 cells per condition.

(G) Increased TIFs specifically in MuSCs. n = 3 mice (5 months old) per genotype. n > 70 cells per condition. All datasets are displayed as mean ± SEM. All statistical analyses were performed using unpaired Student's t test with Welch's correction. *p ≤ 0.05; **p ≤ 0.01.

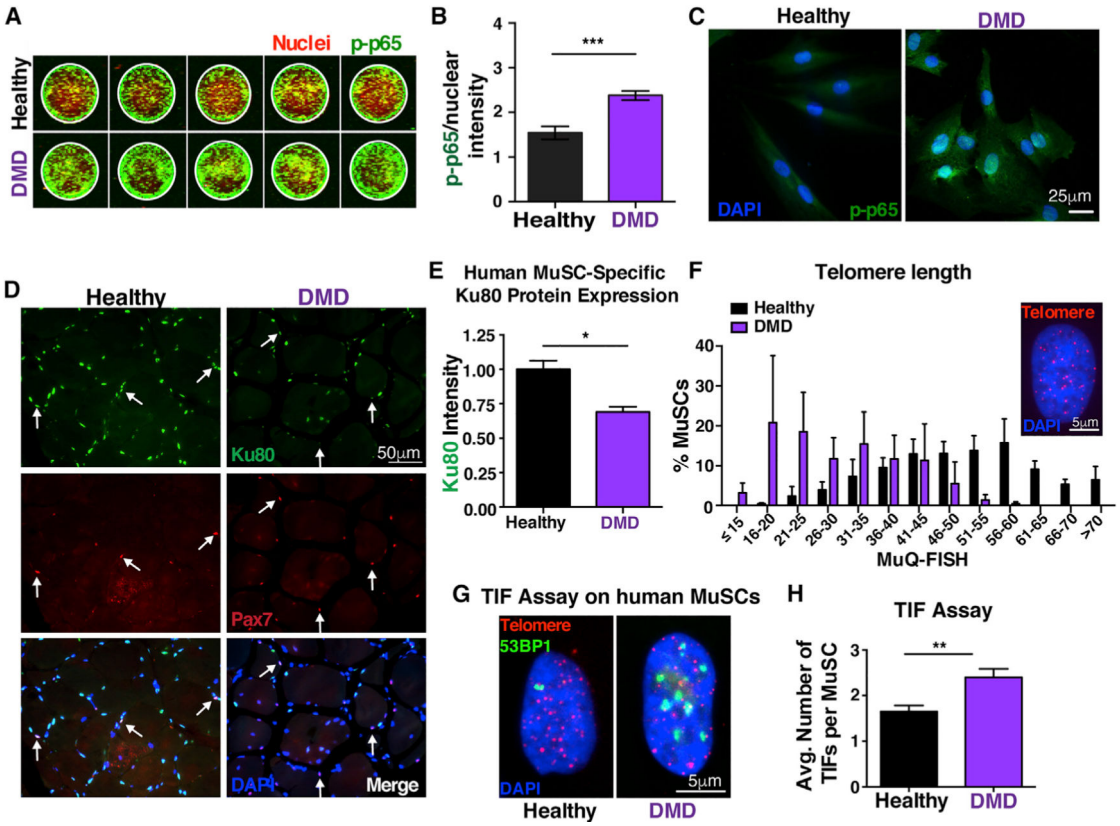

Figure 6. Persistent NF-κB activation in human DMD MuSCs leads to Ku80 dysregulation and predisposes these cells to premature telomere shortening and increased number of TIFs

(A) In-cell western representative image of phospho-p65 staining of human MuSCs. MuSCs from three healthy and three DMD patients 10–15 years old were analyzed with five technical replicates each. Green, phospho-p65 staining; red, Draq5 (nuclear) staining.

(B) Quantification shows nuclear accumulation of p-p65 in hMuSCs. The total signal intensity in the IR 800 channel (p-p65) was normalized to the total intensity of the Draq5 (nuclear channel) per sample. n = 3 samples/group. n = 6 wells per sample.

(C) Higher NF-κB activity in NCAM+ human MuSCs from young DMD patients, as shown by the p-p65 nuclear accumulation compared to age-matched control MuSCs.

(D) n = 3 samples/group. Representative Ku80 staining (green), Pax7 (red), and nuclei (DAPI, blue) in human healthy and DMD muscle sections (21–26 years old).

(E) Quantification shows reduced levels of Ku80 in dystrophic MuSCs compared to controls. n = 3 samples/group. n > 30 cells per sample.

(F) Reduced telomere length in human MuSCs, assessed by MuQ-FISH of telomere staining (insert, representative image). n = 3 samples/group. n > 80 cells per sample.

(G) Representative images of TIF assay in human MuSCs.

(H) Quantification analysis reveals increased number of TIFs in human MuSCs.

n = 3 samples/group. n > 60 cells per sample. Graphed data are displayed as mean ± SEM. Statistical analyses in (B), (E), and (H) were performed using unpaired Student's t test with Welch's correction. *p ≤ 0.05; **p ≤ 0.01; ***p ≤ 0.001.

KEY RESOURCES TABLE

REAGENT or RESOURCE	SOURCE	IDENTIFIER
Antibodies		
anti-Alpha 7 Integrin Alexa Fluor 647, clone R2F2	ablab.ca	Cat# 67-0010-05
Alexa Fluor 488-conjugated mouse anti-phospho-p38 MAPK threonine 180/tyrosine 182	BD Biosciences	Cat# 612594; RRID: AB_399877
Alexa Fluor 488 Donkey anti-goat IgG	Thermo Fisher Scientific	Cat# A11055; RRID:AB_2534102
Alexa Fluor 488 Goat anti-rabbit IgG	Thermo Fisher Scientific	Cat# A-11034; RRID: AB_2576217
Alexa Fluor 488 Goat anti-mouse IgG	Thermo Fisher Scientific	Cat# A-11001; RRID: AB_2534069
Alexa Fluor 555 Donkey anti-goat IgG	Thermo Fisher Scientific	Cat# A21432; RRID:AB_2535853
Alexa Fluor 555 Donkey anti-rabbit IgG	Thermo Fisher Scientific	Cat# A31572; RRID:AB_162543
Alexa Fluor 555 Goat anti-rabbit IgG	Thermo Fisher Scientific	Cat# A21428; RRID:AB_2535849
Alexa Fluor 647-conjugated mouse anti-Ku86	Santa Cruz	Cat# sc-515736 AF645
Alexa Fluor 647 Goat-anti-mouse IgG	Thermo Fisher Scientific	Cat# A-21235; RRID: AB_2535804
Dylight 800-conjugated Goat-anti-rabbit IgG	Rockland	Cat# 611-145-122; RRID:AB_1057618
Goat anti-mouse Vcam1	Fisher Scientific	Cat# PIPA547029
Hamster anti-mouse Bcl2	BD Biosciences	Cat# 556537 RRID:AB_396457
Ki67 antibody	abcam	Cat# ab15580; RRID:AB_443209
Mouse anti-human CD11b	Thermo Fisher Scientific	Cat# 14-0118-82; RRID:AB_467120
Mouse anti-human CD31	Thermo Fisher Scientific	Cat# 14-0319-82; RRID:AB_467204
Mouse anti-human CD45	Thermo Fisher Scientific	Cat# 14-0459-82; RRID:AB_467274
Mouse anti-human NCAM	Thermo Fisher Scientific	Cat# 17-0567-42; RRID:AB_10597454
Mouse anti-Pax7	Santa Cruz	Cat# sc-81648; RRID:AB_2159836
Mouse anti-phospho-SAPK/JNK threonine 183/tyrosine 185	Cell Signaling	Cat# 9255; RRID: AB_2307321
Rabbit anti-53bp1	Novus Biologicals	Cat# NB100-304; RRID:AB_10003037
Rabbit anti-Ku80	Proteintech	Cat# 16389-1-AP; RRID:AB_2257509
Rabbit anti-phospho-Akt serine 473	Cell Signaling	Cat# 4058; RRID:AB_331168
Rabbit anti-phospho-p65 serine 529	abcam	Cat# ab97726; RRID:AB_10681170
Rabbit anti-phospho-p65 serine 536	abcam	Cat# ab86299; RRID:AB_1925243
Rabbit anti-phospho-p65 serine 536	abcam	Cat# ab131109; RRID:AB_11160495
Rabbit anti-phospho-p70 s6 kinase threonine 421/serine 424	Cell Signaling	Cat# 9204; RRID: AB_2265913
Rat anti-CD11b-biotin, clone M1/70	BD Biosciences	Cat# 553309; RRID:AB_394773
Rat anti-CD31-biotin	Fisher Scientific	Cat# 13-0311-85; RRID:AB_466421
Rat anti-mouse CD34-BV421, Clone RAM34	BD Biosciences	Cat# 562608; RRID:AB_11154576
Rat anti-CD45-biotin	BD Biosciences	Cat# 553078; RRID:AB_394608
Rat anti-Ly-6A/E-biotin (Sca1), clone E13-161.7	BD Biosciences	Cat# 553334; RRID:AB_394790
Biological samples		
Primary human MuSCs	From collaborator Tichy et al., 2017	N/A
Human skeletal muscle paraffin sections	Obtained in-house and from US Biomax	N/A

REAGENT or RESOURCE	SOURCE	IDENTIFIER
Chemicals, peptides, and recombinant proteins		
16% paraformaldehyde	Electron Microscopy Sciences	Cat# 15710
2-Mercaptoethanol	Bio-Rad	Cat#1610710
2-Methylbutane	Honeywell	Cat# M32631
4% paraformaldehyde	Thermo Scientific	Cat# J19943-K2
5-Ethynyl-2′-deoxyuridine (EdU)	abcam	Cat# ab146186
7-aminoactinomycin D (7-AAD)	Fisher Scientific	Cat# A1310
Accumax	Fisher Scientific	Cat# SCR006
Acetic Acid, glacial	Fisher Scientific	Cat# A38S
Alcoholic Eosin	American MasterTech Scientific	Cat# STE0157
Antibiotic-antimycotic	GIBCO	Cat# 15240-062
Antigen unmasking solution	Vector Labs	Cat# H-3300
Avidin/Biotin blocking solution	Vector Labs	Cat# SP2001
Bluing	American MasterTech Scientific	Cat# HXB00242E
Bouin's solution	Sigma-Aldrich	Cat# HT10132
Bovine Serum Albumin (Fraction V)	Gemini Bio-Products	Cat# 700-100P
Cenpb-Cy3	PNA Bio	Cat# F3002
Collagen	Sigma-Aldrich	Cat# C8919
Collagenase type 1A	Sigma-Aldrich	Cat# C9891
Corn Oil	Millipore-Sigma	Cat# C8267
Cytoseal-Xyl	Thermo Scientific	Cat# 8312-4
DAPI	Sigma-Aldrich	Cat# D9542
DRAQ5	Biolegend	Cat# 424101
Dextran sulfate sodium salt	Sigma-Aldrich	Cat# D8906
Dispase II	Roche	Cat# 04942078001
DMEM high glucose	Corning	Cat# 10-017-CV
DMEM/F-12	ThermoFisher Scientific	Cat#11330-032
EDTA	Invitrogen	Cat#15575-020
Ethanol, 200 proof	Decon Labs	Cat# 2701
ESGRO-2i	EMD Millipore	Cat# ESG1121
Ethylene Carbonate	Sigma-Aldrich	Cat# E26258
Fetal Bovine Serum	Corning	Cat# MT35-010-CV
Fluoromount G plus DAPI	Southern Biotech	Cat# 0100-20
Formaldehyde solution, 37%	Sigma-Aldrich	Cat# F1635
Formamide	Sigma-Aldrich	Cat# 47670
Gill's Hematoxylin	Cancer Diagnostics	Cat# CM5951
Glutamax	GIBCO	Cat# 35050-061
Igepal CA-630	Sigma-Aldrich	Cat# I8896
Laminin	Sigma-Aldrich	Cat#11243217001
Luria Broth, Miller	Sigma-Aldrich	Cat# L3152
Maleic acid	Sigma-Aldrich	Cat# M0375

REAGENT or RESOURCE	SOURCE	IDENTIFIER
MEM Nonessential amino acids	GIBCO	Cat# 11140-050
Methanol	Fisher Scientific	Cat# A412-4
Magnesium chloride	Sigma-Aldrich	Cat# M8266
Mouse on mouse kit	Vector Labs	Cat# BMK-2202
Normal Goat Serum	ThermoFisher Scientific	Cat# 16210-072
Notexin	Accurate Chemical/Latoxan	Cat# TXL8104-100
OCT	Thermo Scientific	Cat# 6502G
Phosphate buffered saline	Made in house	N/A
Prolong gold plus DAPI	ThermoFisher Scientific	Cat# P36935
Red cell lysis buffer	Invitrogen	Cat# 50-112-9751
Ringers solution	Made in house	N/A
RNase A	Fisher Scientific	Cat# AM9780
SSC buffer, 20X	Corning	Cat# 46-020-CM
Streptavidin Alexa Fluor 488	Biolegend	Cat# 405235
Streptavidin APC-Cy7	BD Biosciences	Cat# 554063
Streptavidin PE-Cy7	Biolegend	Cat# 405206
Tamoxifen	Sigma-Aldrich	Cat# T5648
Taqman universal 2x master mix	Applied Biosystems	Cat# 4304437
TelC-Alexa Fluor 647	PNA Bio	Cat# F1013
TelC-Cy3	PNA Bio	Cat# F1002
Telomere blocking buffer	Millipore-Sigma	Cat# 11096176001
Triton X-100	Fisher Scientific	Cat# BP151
Tris-Cl	Quality Biological	Cat#351-006-131
Trypsin-EDTA	GIBCO	Cat# 25200-056
Tween 20	Fisher Scientific	Cat# BP337
Weigert's Iron Hematoxylin A	Electron Microscopy Sciences	Cat# 26386-02
Weigert's Iron Hematoxylin B	Electron Microscopy Sciences	Cat# 26386-03
Xylene	Fisher Scientific	Cat# X5-4
Critical commercial assays		
Click-iT EdU Alexa Fluor 594 Imaging Kit	Life Technologies	Cat# C10339
Creatine Kinase Assay	Sekisui Diagnostics	Cat# 326-10
Protoscript II cDNA First Strand Synthesis Kit	New England Biolabs	Cat# E6560S
Qiafilter Plasmid Midi Kit	QIAGEN	Cat# 12243
Rneasy Plus Micro Kit	QIAGEN	Cat# 74034
Trichrome Staining Kit	Sigma-Aldrich	Cat# HT15-1KT
Experimental models: Cell lines		
Human MuSCs, primary ($NCAM^+/CD31^-/CD45^-/CD11b^-$)	Collaborator: (Tichy et al., 2017)	N/A
Mouse C2C12 Cells	ATCC	Cat# CRL-1772; RRID:CVCL_0188
Mouse Embryonic Stem Cells (W4)	University of Pennsylvania iPS cell core	RRID:CVCL_Y634

REAGENT or RESOURCE	SOURCE	IDENTIFIER
Experimental models: Organisms/strains		
Mouse: C57BL/6J	Jackson Labs	Stock# 000664; RRID:IMSR_JAX:000664
Mouse: IKK2CA: B6.Cg-*Gt(ROSA)26Sor*$^{tm4(Ikbkb)Rsky}$/J	Jackson Labs	Stock # 008242; RRID:IMSR_JAX:008242
Mouse: Ku80$^{+/-}$	Collaborator: Zhu et al., 1996	N/A
Mouse: mdx^{4cv}: B6Ros.Cg-*Dmd*$^{mdx-4Cv}$/J	Jackson Labs	Stock# 002378; RRID:IMSR_JAX:002378
Mouse: NEMOKO^{Flox}	Described in Schmidt-Supprian et al., 2000	N/A
Mouse: Pax7EGFP	Generated In-house Tichy et al., 2018	N/A
Mouse: Pax7^{ERT2Cre}: B6.Cg-*Pax7*$^{tm1(cre/ERT2)Gaka}$/J	Jackson Labs	Stock # 017763; RRID:IMSR_JAX:017763
Oligonucleotides		
CHUK- FAM	Applied Biosystems	Assay ID# Mm00432529_m1
Gapdh-VIC-MGB	ThermoFisher Scientific	Cat# 4352339e
IKBKB -FAM	Applied Biosystems	Assay ID# Mm01222247_m1
IKBKG-FAM	Applied Biosystems	Assay ID# Mm00494927_m1
POT1B-FAM	Applied Biosystems	Assay ID# Mm01278790_m1
TERF1-FAM	Applied Biosystems	Assay ID# Mm00436928_m1
TERF2-FAM	Applied Biosystems	Assay ID# Mm01253555_m1
TERF2IP-FAM	Applied Biosystems	Assay ID# Mm01243676_m1
TERT-FAM	Applied Biosystems	Assay ID# Mm00436931_m1
TINF2-FAM	Applied Biosystems	Assay ID# Mm00461166_g1
TPP1-FAM	Applied Biosystems	Assay ID# Mm00487016_m1
XRCC5-FAM	Applied Biosystems	Assay ID# Mm00550142_m1
XRCC6-FAM	Applied Biosystems	Assay ID# Mm00487458_m1
Recombinant DNA		
shEmpty (pLKO.1 puro)	Addgene	RRID: Addgene_8453
shXRCC5-1	Sigma-Aldrich	Cat#:SHCLNG-NM_00953; ID#: TRCN0000312925
shXRCC5-2	Sigma-Aldrich	Cat#:SHCLNG-NM_00953; ID#: TRCN0000071044
Software and algorithms		
Fiji	Open Source	https://imagej.net/Fiji
Flowjo v. 10.7.1	Licensed Software	https://www.flowjo.com
Graphpad Prism v. 6.0h	Licensed Software	https://www.graphpad.com
ImageJ	Open Source	https://imagej.net/Welcome
Image Studio	Licensed Software	https://www.licor.com/bio/image-studio/

REAGENT or RESOURCE	SOURCE	IDENTIFIER
Lasagna	Open Source	https://biogrid-lasagna.engr.uconn.edu/lasagna_search/index.php
Leica Application Suite X	Licensed Software	https://www.leica-microsystems.com/products/microscope-software/p/leica-las-x-ls/
NIS-Elements	Licensed Software	https://www.microscope.healthcare.nikon.com/products/software/nis-elements
Odyssey Infared Imaging Software, v. 3.0.30	Licensed Software	https://www.licor.com
Telometer ImageJ Plugin	Open Source	https://demarzolab.pathology.jhmi.edu/telometer/
Zeiss Zen Imaging Software	Licensed Software	https://www.zeiss.com/microscopy/us/products/microscope-software/zen.html
Other		
40 μm cell strainers	VWR	Cat# 10199-654
70 μm cell strainers	Thermo Fisher Scientific	Cat# 08-771-2
96 well plate, black, optical flat bottom	Thermo Fisher Scientific	Cat# 4311971
96 well plate, v bottom	Greiner Bio-One	Cat# 651160
C-tubes	Miltenyi	Cat# 130-096-334
Falcon tube with cell strainer cap	Fisher Scientific	Cat# 0877123
Insulin Syringe	Exel International	Cat# 26028
Lipofectamine 3000	Thermo Fisher Scientific	Cat# L3000008
Nunc Lab-Tek II 8-well chamber slides	Thermo Fisher Scientific	Cat# 125658
Superfrost plus microscope slides	Thermo Fisher Scientific	Cat# 1255015